

# **Atmospheric observations and emissions estimates of methane and nitrous oxide from regional to global scale**

A dissertation presented

by

Eric Adam Kort

to

The School of Engineering and Applied Science

in partial fulfillment of the requirements  
for the degree of

Doctor of Philosophy

in the subject of

Applied Physics

Harvard University  
Cambridge, Massachusetts

February, 2011

© 2011 – Eric Adam Kort  
All rights reserved.

Dissertation Advisor

Author

**Professor Steven C. Wofsy**

**Eric Adam Kort**

## **Atmospheric observations and emissions estimates of methane and nitrous oxide from regional to global scale**

### Abstract

Methane (CH<sub>4</sub>) and Nitrous Oxide (N<sub>2</sub>O) are the two most significant anthropogenic, long-lived, non-CO<sub>2</sub> greenhouse gases, together perturbing the earth's energy balance by an amount comparable to that of CO<sub>2</sub>, **but their source distribution, magnitude, and seasonality remain poorly quantified.** This dissertation will focus on the use of atmospheric observations to quantify emissions of CH<sub>4</sub> and N<sub>2</sub>O. First, top-down emissions constraints on the regional scale, covering large areas of the U.S and southern Canada, are derived from airborne observations made in Spring of 2003. Using a receptor-oriented Lagrangian particle dispersion model provides robust validation of bottom-up emission estimates from EDGAR 32FT2000 and GEIA inventories. It is found that EDGAR CH<sub>4</sub> emission rates are slightly low by a factor of  $1.08 \pm 0.15$  ( $2 \sigma$ ), while both EDGAR and GEIA N<sub>2</sub>O emissions are significantly too low, by factors of  $2.62 \pm 0.50$  and  $3.05 \pm 0.61$  respectively. This analysis is then extended over a full calendar year in 2004 with observations from NOAA's tall tower and aircraft profile network. EDGAR 32FT2000 CH<sub>4</sub> emissions are found to be consistent with observations, though the newer EDGAR v4.0 reduces CH<sub>4</sub> emissions by 30%, and this reduction is not consistent with this study. Scaling factors found for N<sub>2</sub>O in May/June of 2003 are found **???** to hold for February-May of 2004, suggesting inventories are significantly too low in primary growing season coincident with significant fertilizer inputs. **.PP** A new instrument for airborne observation of CO<sub>2</sub>, CH<sub>4</sub>, N<sub>2</sub>O, and CO is introduced, and its operation and

in-field performance **are** highlighted (demonstrated 1-sec precisions of 20 ppb, 0.5 ppb, 0.09 ppb, and 0.15 ppb respectively). Finally, global N<sub>2</sub>O observations collected **with this sensor** on the HIPPO (HIAPER Pole to Pole Observations) campaign are assessed. Comparison with a global model and subsequent inversion indicates <sup>strong, episodic inputs of nitrous</sup> ~~significant bursts of tropical nitrous~~ <sub>oxide from tropical regions</sub> oxide emissions are necessary to bring observations and model in agreement. Findings highlight the strong temporal variability of nitrous oxide emissions, and the necessity of using full vertical profile observations in deriving emissions from atmospheric measurements.

# Contents

Abstract.....	iii
Table of Contents.....	v
List of Figures.....	viii
List of Tables.....	ix
Acknowledgements.....	x
<b>Chapter 1: Overview.....</b>	<b>1</b>
1.1 Non-CO <sub>2</sub> greenhouse gases.....	1
1.2 Research questions and methods.....	3
1.3 Dissertation outline and major results.....	3
<b>Chapter 2: Emissions of CH<sub>4</sub> and N<sub>2</sub>O over the United States and Canada based on a receptor-oriented modeling framework and COBRA-NA atmospheric observations.....</b>	<b>8</b>
2.1 Introduction.....	9
2.2 Study & Measurements.....	10
2.3 Methodology.....	11
2.3.1 Meteorological Input and Footprint Estimation.....	11
2.3.2 Emissions Inventories.....	12
2.3.3 Upwind Boundary Condition.....	13
2.3.4 Assessment/Optimization Approach.....	13
2.4 Results and Discussion.....	14
2.4.1 Methane.....	14
2.4.2 Nitrous Oxide.....	15
2.5 Conclusion.....	17
2.6 Acknowledgements.....	18
2.7 Supplemental Materials.....	18
2.7.1 Sampling Method.....	18
2.7.2 WRF runs.....	20
2.7.3 Boundary Condition.....	20
2.7.4 Measurement Uncertainty.....	21
2.7.5 Model Uncertainty.....	21
2.7.6 Possible Footprint Bias.....	22
2.7.7 Considering Uncertainties.....	23
<b>Chapter 3: Atmospheric constraints on 2004 emissions of methane and nitrous oxide in North America from atmospheric measurements and a receptor-oriented modeling framework.....</b>	<b>29</b>
3.1 Introduction.....	30
3.2 Measurements.....	30
3.3 Methodology.....	31
3.3.1 Meteorological Input.....	31

3.3.2 Footprint Estimation, Emissions Inventories, and Upwind Boundary Condition.....	32
3.3.3 Optimization Approach.....	33
3.4 Results: Methane.....	34
3.4.1 Briggsdale, Colorado (CAR).....	34
3.4.2 Park Falls, Wisconsin (LEF).....	34
3.4.3 Worcester, Massachusetts (NHA).....	36
3.4.4 Boundary Condition.....	36
3.4.5 Source Partitioning.....	36
3.5 Results: Nitrous Oxide.....	37
3.6 Conclusion.....	38
3.7 Acknowledgements.....	39

**Chapter 4: Instrumentation: Airborne Observations of Carbon Dioxide, Carbon Monoxide, Methane, and Nitrous Oxide..... 44**

4.1 Introduction.....	45
4.2 Instrument Design.....	
4.2.1 QCO <sub>2</sub> .....	
4.2.2 DUAL.....	
4.3 Instrument Operation.....	
4.3.1 Calibration.....	
4.4 Performance.....	
4.5 In-flight instrument comparison.....	
4.6 Conclusion.....	

**Chapter 5: Nitrous oxide’s tropospheric variability: evidence for strong tropical emissions..... 63**

5.1 Introduction.....	64
5.2 Model & Measurements.....	
5.3 Results & Discussion.....	
5.4 Conclusion.....	
5.5 Acknowledgments.....	
5.6 Supplemental Materials.....	
5.6.1 HIPPO campaign, deployments 1 & 2.....	
5.6.2 QCLS.....	
5.6.3 Inversion Technique.....	

## List of Figures

## List of Tables

## **Acknowledgements**

Thanks yous etc...

## CHAPTER 1

### Overview

#### 1.1 Non-CO<sub>2</sub> greenhouse gases

The earth's atmosphere is presently experiencing a significant compositional change driven by human activities. Rapidly increasing concentrations of greenhouse gases are perturbing the earth's energy balance, leading to an increase in global surface temperature. This global warming has become one of the defining issues of our time, and is at the center of much political discourse. Much of the scientific and political rhetoric on global warming is centered on Carbon Dioxide (CO<sub>2</sub>), the single largest anthropogenic contributor to radiative forcing (change in earth's energy balance) since preindustrial times. This attention is warranted, but often overshadows the fact that non-CO<sub>2</sub> greenhouse gases have contributed a comparable amount to radiative forcing since pre-industrial times (1 W/m<sup>2</sup> compared to 1.6 W/m<sup>2</sup> for CO<sub>2</sub> in 2004) [Hofmann et al., 2006]. As Shine and Sturges [2007] have so elegantly phrased "CO<sub>2</sub> Is Not the Only Gas".

Long-lived, anthropogenic, non-CO<sub>2</sub> greenhouse gases are led by methane (CH<sub>4</sub>) and nitrous oxide (N<sub>2</sub>O), having the first and second largest contribution to radiative forcing respectively (<http://www.esrl.noaa.gov/gmd/aggi/>). In addition to direct climate effects of CH<sub>4</sub> and N<sub>2</sub>O in the troposphere, both gases have important stratospheric influence. Destruction of CH<sub>4</sub> by the hydroxyl radical (OH) is the primary source of water vapor in the stratosphere, with significant radiative and chemical impacts (notably surface warming and stratospheric ozone destruction) [Forster and Shine, 1999]. With the reduction of CFC emissions, it has now been claimed that N<sub>2</sub>O (as a source of nitric

oxide (NO) to the stratosphere) is the dominant ozone-depleting substance in this century [Ravishankara et al., 2009]. Despite the importance of methane and nitrous oxide in the earth's atmosphere, we still have relatively poor knowledge of their source distributions, magnitudes, and seasonality.

Atmospheric methane originates from a **wide** variety of sources, both anthropogenic and natural. Natural sources comprise ~35% of present day methane emissions. By far the largest, and most uncertain source is wetlands, estimated to contribute 100-230 Tg CH<sub>4</sub>/yr (total annual natural 145-260 Tg CH<sub>4</sub>/yr) [Denman et al., 2007]. Remaining natural sources include termites, the ocean, hydrates, geological sources, wild animals, and wildfires. Anthropogenic sources total 264-428 Tg CH<sub>4</sub>/yr [Denman et al., 2007], with contributions from coal mining, the gas & oil industry, landfills, ruminants, rice agriculture, and biomass burning. By far the dominant sink is tropospheric OH, though there is some methane consumed by soils and some lost to the stratosphere. The present atmospheric **turnover time** of CH<sub>4</sub> is ~ 9 years. Methane has increased by a factor of 2.5 since 1800, with this rapid increase driven by anthropogenic emissions. Since 1990 the growth rate of atmospheric methane has dropped and exhibited large interannual variations. Various explanations exist for the variability and decline in growth rate, pointing either towards fossil fuels, biomass burning, and/or wetlands [Bousquet et al., 2006; Dlugokencky et al., 1994; Simpson et al., 2006]. There is some indication the growth rate is on the rise again [Rigby et al., 2008], but present data is not inconsistent with the notion that atmospheric methane is reaching a steady-state [Dlugokencky et al., 2009].

Atmospheric nitrous oxide also originates from both natural and anthropogenic sources. Natural sources of N<sub>2</sub>O are predominantly from soils (3.3-9 Tg N/yr), though the ocean also contributes (1.8-5.8 Tg N/yr). Anthropogenic sources are dominated by agriculture (from fertilizer application), contributing 1.7-4.8 Tg N/yr. Other, much smaller anthropogenic sources include fossil fuel combustion, industrial processes, and biomass burning. The predominant sink for N<sub>2</sub>O is photolysis in the stratosphere.

Atmospheric values have risen from 270 ppb in preindustrial times to 319 ppb in 2005 and continue to increase at a linear rate of  $\sim 1$  ppb/yr [Denman et al., 2007].

## 1.2 Research questions and methods

This work aims to directly use atmospheric observations to improve emissions estimates of CH<sub>4</sub> and N<sub>2</sub>O. Central to this work are the big picture questions:

- What are regional to global scale emissions of methane and nitrous oxide?
- What is the spatial-temporal variation of these emissions?

I address these questions with a combination of atmospheric observations, emissions inventories, and atmospheric models ranging from the regional to global scale. Observations used include flask samples collected over North America both from aircraft and tall towers, in addition to high resolution, global, *in-situ* observations made from aircraft. For regional to continental scales, I use a high resolution Lagrangian Particle Dispersion Model (LPDM), while on the global scale a 3-D atmospheric chemical transport model is used. By directly linking observations with inventories via atmospheric transport models, tight constraints on emissions can be found. Looking at varied spatial-temporal scales then further elucidates emission behavior.

## 1.3 Dissertation outline and major results

Chapter 2 presents the first application of a LPDM to estimate emissions of CH<sub>4</sub> and N<sub>2</sub>O. This work demonstrates that transport models are now sufficiently accurate for using atmospheric observations to constraining regional CH<sub>4</sub> and N<sub>2</sub>O emissions. Using airborne measurement collected in Spring of 2003, it is found that for methane, the EDGAR 32FT2000 [Olivier et al., 2005] inventory is consistent with observations (slightly low), while both EDGAR and GEIA [Bouwman et al., 1995] are significantly

low for nitrous oxide (by factors of 2.5-3). Such a large discrepancy has large implications for North American emissions, but the seasonality of these emissions may reduce the large predicted increase in inventory emissions.

In Chapter 3 I extend this analysis to capture a full seasonal cycle in 2004 by using observations from NOAA's tall tower and aircraft profile network. For methane, EDGAR 32FT2000 is found to be slightly low compared with observations (20-30%), but the newly released EDGAR v4.0 reduces US emissions a further 30%, consistent with EPA reported emissions, but significantly low compared to [results here](#). For nitrous oxide, it is found that the large scaling factors found for May/June of 2003 from aircraft data improve model data agreement when applied to tower data for February through May, consistent with peak emissions arising from agricultural regions such as the Midwest.

Chapter 4 introduces new instrumentation, QCLS (Quantum Cascade Laser Spectrometer) for airborne observation of carbon dioxide, methane, nitrous oxide, and carbon monoxide. The fast time response and high precision and accuracy of the instrument enables the collection of fine-grained observations for all four gases, improving observational constraints on emissions.

Chapter 5 makes use of global observations collected with QCLS on the first two HIPPO (HIAPER Pole to Pole Observations) campaigns, spanning altitudes from the surface to 14 km and latitudes from 67°S to 85°N. Comparisons with a 3-D global atmospheric chemical transport model expose the failure of models to accurately capture the vertical distribution of nitrous oxide. Inverse analysis indicates strong pulses of tropical nitrous oxide emissions (as large as 1 Tg N) are necessary to bring model and observations in agreement. Findings highlight the strong temporal variability of nitrous oxide emissions [the deficiencies of conventional inversion](#) approaches based solely on surface observations.

Taken collectively, these findings emphasize the large uncertainty in non-CO<sub>2</sub> greenhouse gas emissions. New instrumentation and current atmospheric models are both



of sufficient quality to assess and attribute changes in atmospheric mole fractions of a fraction of a percent to emissions. These observations and modeled analyses show that emissions can be three times larger than predicted, and that unexpected large temporal variations in fluxes on weekly to seasonal time frames occur. Increased observations of high precision and with continuous temporal coverage near poorly constrained source regions (i.e. mid-latitude agriculture and tropical soils) would be invaluable to improving our knowledge of emissions, and an essential step before atmospheric observations of non-CO<sub>2</sub> greenhouse gases could be used to verify anthropogenic emissions in any future international agreement.



## References Cited

- Bousquet, P., et al. (2006), Contribution of anthropogenic and natural sources to atmospheric methane variability, *Nature*, 443(7110), 439-443.
- Bouwman, A.F., K.W. van der Hoek and J.G.J. Olivier (1995), Uncertainties in the global source distribution of N<sub>2</sub>O, *J. Geophys. Res.*, 100(D2), 2785-2800.
- Denman, K.L., G. Brasseur, A. Chidthaisong, P. Ciais, P.M. Cox, R.E. Dickinson, D. Hauglustaine, C. Heinze, E. Holland, D. Jacob, U. Lohmann, S Ramachandran, P.L. de Silva Dias, S.C. Wofsy, and X. Zhang, 2007: Couplings Between Changes in the Climate System and Biogeochemistry. In: *Climate Change 2007: The Physical Science Basis. Contribution of Working Group I to the Fourth Assessment Report of the Intergovernmental Panel on Climate Change* [Solomon, S., D. Qin, M. Manning, Z. Chen, M. Marquis, K.B. Averyt, M. Tignor and H.L. Miller (eds.)]. Cambridge University Press, Cambridge, United Kingdom and New York, NY, USA.
- Dlugokencky, E. J., K. A. Masarie, P. M. Lang, P. P. Tans, L. P. Steele, and E. G. Nisbet (1994), A DRAMATIC DECREASE IN THE GROWTH-RATE OF ATMOSPHERIC METHANE IN THE NORTHERN-HEMISPHERE DURING 1992, *Geophysical Research Letters*, 21(1), 45-48.
- Dlugokencky, E. J., et al. (2009), Observational constraints on recent increases in the atmospheric CH<sub>4</sub> burden, *Geophysical Research Letters*, 36.
- Forster, P. M. D., and K. P. Shine (1999), Stratospheric water vapour changes as a possible contributor to observed stratospheric cooling, *Geophysical Research Letters*, 26(21), 3309-3312.
- Hofmann, D. J., J. H. Butler, E. J. Dlugokencky, J. W. Elkins, K. Masarie, S. A. Montzka, and P. Tans, (2006): The role of carbon dioxide in climate forcing from 1979 - 2004: Introduction of the Annual Greenhouse Gas Index, *Tellus, Ser. B*, 58, 614-619.
- Olivier, J.G.J., Van Aardenne, J.A., Dentener, F., Ganzeveld, L. and J.A.H.W. Peters (2005), Recent trends in global greenhouse gas emissions: regional trends and spatial distribution of key sources. In: "Non-CO<sub>2</sub> Greenhouse Gases (NCGG-4)", A. van Amstel (coord.), page 325-330. Millpress, Rotterdam, ISBN 90 5966043 9.
- Ravishankara, A. R., J. S. Daniel, and R. W. Portmann (2009), Nitrous Oxide (N<sub>2</sub>O): The Dominant Ozone-Depleting Substance Emitted in the 21st Century, *Science*, 326(5949), 123-125.
- Rigby, M., et al. (2008), Renewed growth of atmospheric methane, *Geophysical Research Letters*, 35(22).
- Shine, K. P., and W. T. Sturges (2007), Atmospheric science - CO<sub>2</sub> is not the only gas, *Science*, 315(5820), 1804-1805.

Simpson, I. J., F. S. Rowland, S. Meinardi, and D. R. Blake (2006), Influence of biomass burning during recent fluctuations in the slow growth of global tropospheric methane, *Geophysical Research Letters*, 33(22).

## CHAPTER 2

### **Emissions of CH<sub>4</sub> and N<sub>2</sub>O over the United States and Canada based on a receptor-oriented modeling framework and COBRA-NA atmospheric observations**

[Kort, E. A., J. Eluszkiewicz, B. B. Stephens, J. B. Miller, C. Gerbig, T. Nehrkorn, B. C. Daube, J. O. Kaplan, S. Houweling, and S. C. Wofsy (2008), Emissions of CH<sub>4</sub> and N<sub>2</sub>O over the United States and Canada based on a receptor-oriented modeling framework and COBRA-NA atmospheric observations, *Geophys. Res. Lett.*, 35, L18808, doi:10.1029/2008GL034031.]

#### **Abstract**

We present top-down emission constraints for two non-CO<sub>2</sub> greenhouse gases in large areas of the U.S. and southern Canada during early summer. Collocated airborne measurements of methane and nitrous oxide acquired during the COBRA-NA campaign in May-June 2003, analyzed using a receptor-oriented Lagrangian particle dispersion model, provide robust validation of independent bottom-up emission estimates from the EDGAR and GEIA inventories. We find that the EDGAR CH<sub>4</sub> emission rates are slightly low by a factor of  $1.08 \pm 0.15$  ( $2\sigma$ ), while both EDGAR and GEIA N<sub>2</sub>O emissions are significantly too low, by factors of  $2.62 \pm 0.50$  and  $3.05 \pm 0.61$ , respectively, for this region. Potential footprint bias may expand the statistically retrieved uncertainties. Seasonality of agricultural N<sub>2</sub>O emissions may help explain the discrepancy. Total anthropogenic U.S. and Canadian emissions would be 49 Tg CH<sub>4</sub> and 4.3 Tg N<sub>2</sub>O annually, if these inventory scaling factors applied to all of North America.

## 2.1 Introduction

Knowledge of greenhouse gas emissions is central to understanding the Earth's climate system. Though CO<sub>2</sub> is the single most important anthropogenic greenhouse gas, non-CO<sub>2</sub> anthropogenic greenhouse gases play a significant role in the Earth's energy balance, contributing nearly as much to radiative forcing (RF) as carbon dioxide (0.977 W/m<sup>2</sup> compared to 1.626 W/m<sup>2</sup> in 2004) [Hofmann et al., 2006]. Of non-CO<sub>2</sub> anthropogenic greenhouse gases, CH<sub>4</sub> has the largest RF, while N<sub>2</sub>O has the third-largest RF [Hofmann et al., 2006].

Recently, increased attention has been focused on assessing CH<sub>4</sub> sources. Global atmospheric inversions [Bergamaschi et al., 2007; Chen and Prinn, 2006] and global emissions sensitivity tests [Houweling et al., 2006] have begun to tighten atmospheric constraints on CH<sub>4</sub> sources, though capabilities are limited on a regional (104 km<sup>2</sup>-106 km<sup>2</sup>) scale due reliance on data from remote sites and coarse meteorological resolution (typically 1° x 1° or larger). These shortcomings can be overcome using a regionally focused approach, as taken in the Amazon by Miller et al. [2007]. Global studies of N<sub>2</sub>O have focused on agricultural and industrial emissions from seasonal to interannual time scales [Nevison et al., 2007; Hirsch et al., 2006; Prinn et al., 1990], but have not attempted to place strong constraints on regional budgets.

In this paper, we constrain emissions of CH<sub>4</sub> and N<sub>2</sub>O over large areas of the U.S. and southern Canada using models and data specifically designed to address regional scales at high spatial and temporal resolution. We employ a Lagrangian particle diffusion model (LPDM) to directly connect atmospheric measurements with surface fluxes in a receptor-oriented framework. Our measurements consist of flask samples collected during the CO<sub>2</sub> Boundary Layer Regional Airborne–North America (COBRA-NA) campaign in May and June 2003. A direct comparison of simulations with atmospheric measurements on a fine, regional scale enables us to avoid many of the problems that hamper global inversions, extending methods and applications of LPDMs to regional

studies of surface emissions (e.g. Stohl et al., 2003; Gerbig et al., 2003; Matross et al., 2007; Gimson and Uliasz, 2003).

## 2.2 Study & Measurements

The COBRA-NA campaign consisted of 38 flight legs < 4 hours, from 23 May 2003 through 28 June 2003 (for details see Hurst et al. [2006]). Extensive vertical profiling in well-mixed conditions (avoiding frontal and convective activity) was targeted to collect an appropriate data set for assessing surface emissions of measured gases. Locations of the ~300 flasks collected and used in this study, and their collective footprint, can be found in Figure 2.1. These flasks were analyzed for CO<sub>2</sub>, CO, CH<sub>4</sub>, H<sub>2</sub>, SF<sub>6</sub>, and N<sub>2</sub>O concentrations, and for O<sub>2</sub>/N<sub>2</sub>, Ar/N<sub>2</sub>, 13C in CO<sub>2</sub>, and 18O in CO<sub>2</sub> ratios.

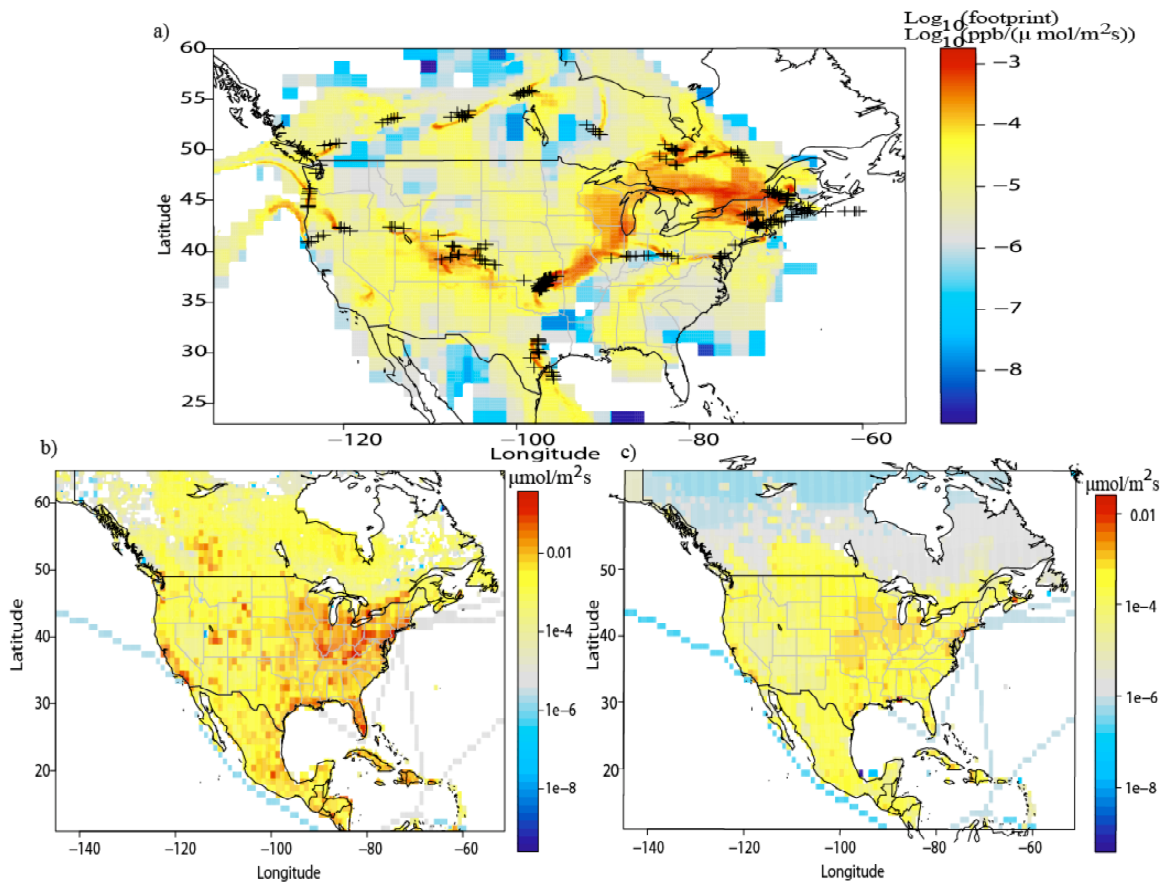


**Figure 2.1** (a) Plus markings indicate locations of airborne flask collection. The average footprint from all the flasks is shown, indicating regions to which our measurements are most sensitive. (b) CH<sub>4</sub> emissions in North America in June (EDGAR and JK). (c) N<sub>2</sub>O emissions in North America (EDGAR).

The CH<sub>4</sub> and N<sub>2</sub>O measurements used here are calibrated on the NOAA2004 [Dlugokencky et al., 2005] and NOAA2006 [Hall et al., 2007] scales, respectively. Further details of flask sampling can be found in the supplemental materials.

## **2.3 Methodology**

The LPDM employed in our work is the Stochastic Time Inverted Lagrangian Transport (STILT) model, run in the time-reversed (receptor-oriented) mode. STILT has been developed and applied to regional emission of CO<sub>2</sub> previously, as described by Lin et al., 2003, Gerbig et al., 2003, and Matross et al., 2007.

### **2.3.1 Meteorological Input and Footprint Estimation**

We drove STILT with meteorological fields from the Weather Research and Forecasting (WRF) model [Skamarock et al., 2005]. We modified WRF to output time-averaged mass fluxes (rather than instantaneous advective velocities) to drive STILT, which results in very good mass conservation (a critical consideration for surface flux estimates), and we also obtained WRF convective mass fluxes that are used directly in STILT. We employed 40-km resolution in WRF version 2.2 that includes analysis nudging to improve meteorological realism. Effects of turbulence in the Planetary Boundary Layer are represented as a Markov chain process [Lin et al., 2003].

Given input meteorological data, the STILT model transports ensembles of 100 particles (air parcels) backwards in time 6 days for the set of ~300 receptor points; advecting particles further back in time increases the fraction of particles to reach the boundary, but going beyond 6 days has no effect on the footprint, and an insignificant effect on boundary values of the gases considered here. For each receptor, we calculate the footprint, which represents the sensitivity of the receptor point to surface sources, in units of ppb/( $\mu\text{mol m}^{-2} \text{s}^{-1}$ ). The footprint is calculated by counting the number of particles in a surface-influenced region (defined as  $\frac{1}{2}$  of the estimated PBL height,

[Gerbig et al., 2003]) and the time spent in the region (for details, see Lin et al., [2003]). The footprint is multiplied by an a priori emission field to compute the associated contribution to the mixing ratio at the receptor.

### **2.3.2 Emissions Inventories**

We need to represent sources and sinks that affect atmospheric concentrations on regional spatial and temporal scales. For CH<sub>4</sub>, we include natural wetland and anthropogenic sources in our a priori emission estimates. Wetland sources are given by the ‘JK’ wetland inventory described in Bergamaschi et al. [2007], indexed on a ½° x ½° grid and changing monthly. Anthropogenic sources are from the EDGAR 32FT2000 inventory [Olivier et al., 2005] (available on a 1° x 1° grid, constant in time). See Figure 2.1b for spatial distribution of emissions.

For N<sub>2</sub>O, two different inventories are used, EDGAR 32FT2000 and GEIA [Bouwman et al., 1995]. EDGAR includes all anthropogenic sources of N<sub>2</sub>O, but does not include natural sources. GEIA includes both natural and anthropogenic sources. Both N<sub>2</sub>O inventories are held constant in time and are available on 1° x 1° grids. See Figure 2.1c for spatial distribution of EDGAR emissions.

Emissions categories for GEIA include soils (natural and agricultural), animal excreta, post-forest clearing enhanced soil emissions, agricultural waste burning, biofuels, fossil fuels, industrial sources, and ocean emissions. EDGAR categories for both CH<sub>4</sub> and N<sub>2</sub>O include fossil fuels, biofuels, industrial sources, agricultural sources, and waste handling. Seasonal factors for the different source categories in EDGAR exist for testing purposes, but the majority of the sources considered here do not exhibit strong temporal variation, and large uncertainty exists in these estimates, so they are not included. The exception is agricultural emissions of N<sub>2</sub>O, and seasonal factors are considered here as discussed in section 4.2.

### 2.3.3 Upwind Boundary Condition

To compare with measurements, the mixing ratio enhancements due to surface fluxes must be added to a background mixing ratio advected from the domain boundary. We retrieve background mixing ratios from a two-dimensional (latitude, height), temporally-varying array placed at 145°W longitude. Mixing ratios are attributed to particles as they cross this boundary. If particles do not reach the boundary, they are given a background mixing ratio taken from the 145°W boundary at the same latitude and altitude as the particle location 6 days traveled back in time. For CH<sub>4</sub>, TM3 “scenario one” model output as described in Houweling et al. [2006] is used for the boundary, shifted down by 27 nmol/mol. This bias is found by comparing model with COBRA-NA measurements above 3km where surface emissions are found to have minimal influence on weekly timescales (on average less than 5 nmol/mol, for methane). It is also consistent with the known offset of ~20 nmol/mol found by Houweling et al. [2006].

Neither data nor global model results are available to set a boundary condition for N<sub>2</sub>O. We plotted the observed N<sub>2</sub>O vs. CH<sub>4</sub> above 3km, where surface influence is small, to determine the ratio of N<sub>2</sub>O variations vs. CH<sub>4</sub> at the boundary (0.010). We then multiplied the CH<sub>4</sub> boundary values by this factor and added the relevant intercept, 299.8 nmol/mol. Using our prior fluxes, variation in background is responsible for 57% of the variation for methane, and 50% of the variation for nitrous oxide.

### 2.3.4 Assessment/Optimization Approach

We fit model results to observations including uncertainty in both x and y, using the  $\chi^2$  (fitxy) method of Press et al., [1992], to ensure unbiased fit parameters [Miller and Tans, 2003]. We assume that errors in the prior sources are constant in space and time, and find one scaling factor (inverse of the fit slope) for the entire emissions field, providing a simple and straightforward approach to assess model performance and determine the North American budgets. We do not have sufficient data to decouple

different source-types or to examine inventory errors in smaller spatial regions. The intercept of the fit, representing a correction to the boundary condition, has little or no effect on the scaling factor. Further information on the effect of the boundary, chi-square optimization, and uncertainties (including footprint bias), is given in the supplemental materials.

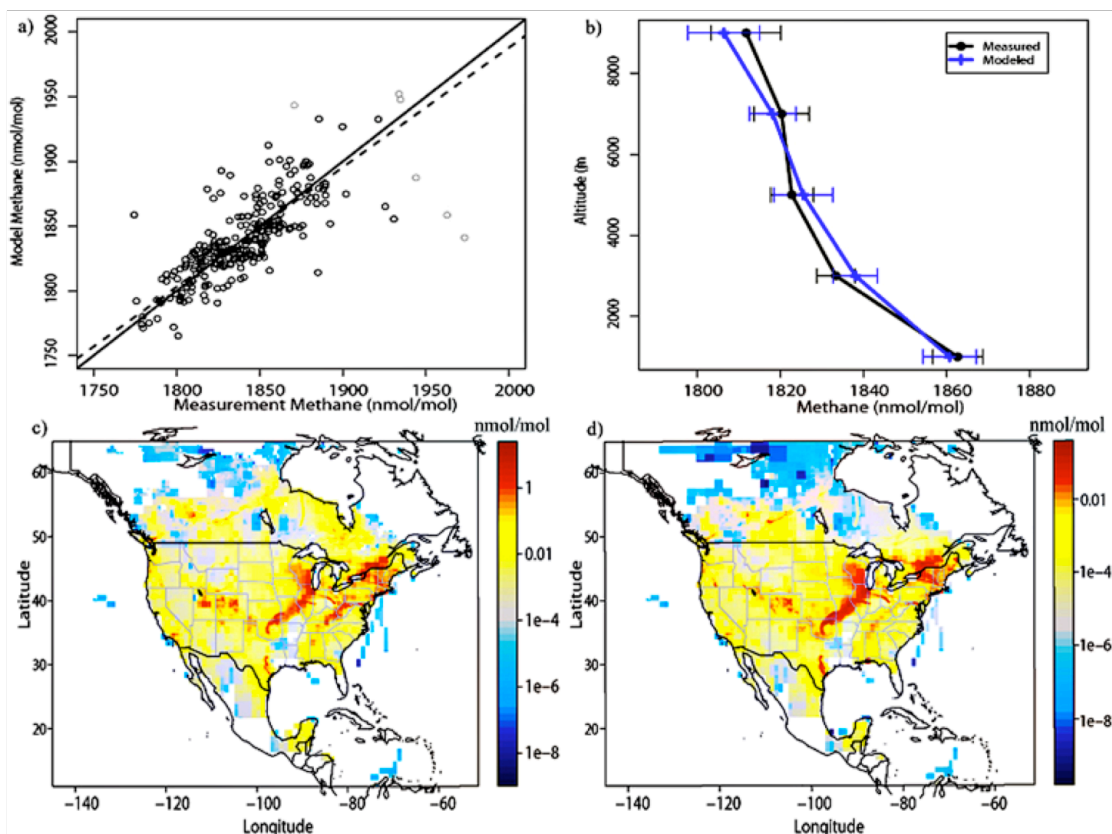


**Figure 2.2** (a) Model vs. measurement for CH<sub>4</sub>, solid line is 1:1 line, dashed line is fit. Grayed points are outliers not included in fit ( $>3\sigma$  from the mean). (b) Bin-averaged vertical distribution showing scaled model in blue, and measurements in black, whiskers illustrate 95% confidence intervals. (c) Total missions footprint multiplied by CH<sub>4</sub> emissions, showing surface contribution to receptor points. (d) Surface contribution of N<sub>2</sub>O to receptor points.

## 2.4 Results and Discussion

### 2.4.1 Methane

Results for CH<sub>4</sub> are remarkable in the point-by-point agreement between

simulated and measured mixing ratios (Figure 2.2a; Figure 2.4b), with a fitted slope remarkably close to one ( $0.924 \pm 0.13$ ), implying a scaling factor for the inventory of  $1.08 \pm 0.15$  (note potential unaccounted footprint bias may expand the uncertainty). Applying the scaling factor to the emissions gives the vertical distribution illustrated in Figure 2.2b; the very good agreement suggests that the WRF-driven STILT model is able to accurately connect measurement locations with source regions upstream, and thus to faithfully model the vertical distribution of CH<sub>4</sub> in the atmosphere—a critical indicator of surface emissions. The agreement above 3km indicates that the advected boundary condition is sufficiently accurate for our purposes. The fidelity of the model to the observations also suggests accuracy in the spatial distribution of the prior emissions inventory, though potentially cancelling errors or footprint bias cannot be ruled out (discussed further in supplement). Anthropogenic sources dominate the inventory in the region that we sampled: fossil fuels, waste handling, and agriculture produce 97% of the total modeled enhancement. Natural wetlands are hardly represented (< 3% total modeled enhancement) in our measurements, and so our assessment of the inventory is restricted to anthropogenic emissions. Spatially, we are sensitive to the high emissions regions in the northern Midwest and Northeast, but not to the large emissions from the gulf coast region (Figure 2.2c).

#### **2.4.2 Nitrous Oxide**

Results for N<sub>2</sub>O are shown in Figure 2.3. Simulations based on the GEIA and EDGAR inventories are very similar, with both simulations underestimating atmospheric measurements. Fitting model vs. EDGAR yields a slope of  $0.381 \pm 0.072$  and vs. GEIA a slope of  $0.328 \pm 0.065$ . Increasing emissions by factors of  $2.62 \pm 0.50$  and  $3.05 \pm 0.61$  for EDGAR and GEIA, respectively, improves model-measurement agreement in the shape of the vertical profile (see Figure 2.3c and 2.3d for the EDGAR inventory). The offset above 3 km is likely caused by the upwind boundary condition. Though the slope

from the 1km to 3 km bin appears somewhat steeper in the measurement than the model, the upper error bound on the scaling, seen in gray, nearly captures the same trend. There is a potential that vertical mixing errors could bias the analysis, though the methane results suggest otherwise. A more likely cause is the advected boundary condition, though consistency between model and measurement, when considering error bounds, suggests the effect on our analysis is small. Spatially, we have coverage of the strong emissions regions through the Midwest and the Northeast (Figure 2.2d).

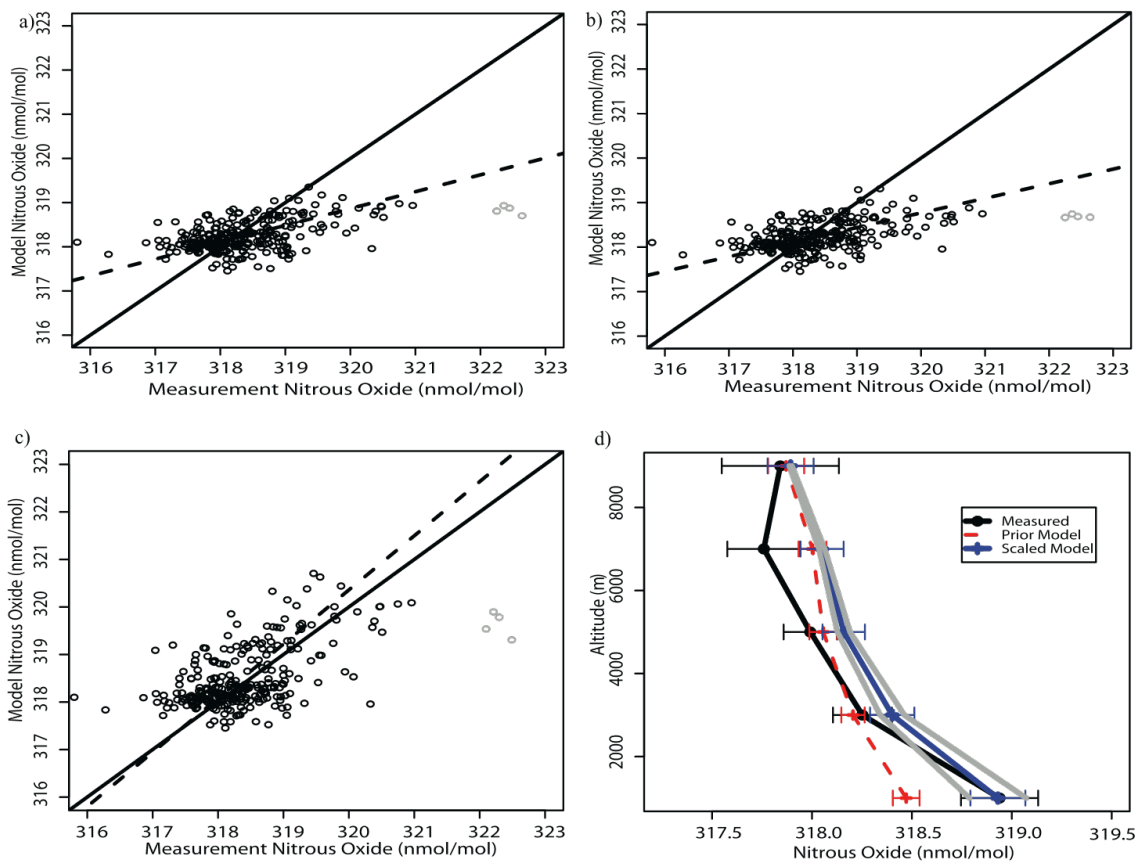


**Figure 2.3** (a) Model vs. measurement for N<sub>2</sub>O, EDGAR case, solid line is 1:1 line, dashed line is fit. Grayed points are outliers not included in fit ( $>3\sigma$  from the mean) (b) GEIA case. (c) EDGAR case scaled by found multiplier (2.62). (d) Binned vertical distribution showing un-scaled model (EDGAR case) in red, scaled model in blue, scaled model with upper and lower bounds on scaling factor in gray, and measurements in black, whiskers illustrate 95% confidence intervals.

These results indicate that in early summer current inventories give N<sub>2</sub>O emissions too low by a factor of 2-3 for much of the USA and southern Canada. Since agricultural emissions dominate the source signal, seasonality may explain some of the under-representation. But applying the published seasonal factors from EDGAR would actually worsen agreement, as the scaling factor for May and June is 0.85. However, the peak scaling factor, for March, is 2.35. If agricultural emissions peaked in May-June instead of March, then our results would be consistent with the EDGAR inventory scaled by this earlier seasonal peak, and the overall annual emissions might not be higher by the indicated factor.

## 2.5 Conclusion

This study simultaneously estimated continental-scale surface fluxes of two important greenhouse gases, CH<sub>4</sub> and N<sub>2</sub>O, using a top-down approach built upon the STILT LPDM, constrained by collocated atmospheric measurements from aircraft and optimized with a simple regression approach. Results suggest the EDGAR inventory for CH<sub>4</sub> accurately accounts for emissions over much of the U.S. and southern Canada (accurate to  $8 \pm 14\%$ ). In contrast, N<sub>2</sub>O emissions in both EDGAR and GEIA are underestimated (by factors of  $2.62 \pm 0.50$  and  $3.05 \pm 0.61$ , respectively). Potential footprint bias may expand uncertainty but we believe this effect to be small (supplement). Seasonality in agricultural emissions could be responsible for the discrepancy. However, if seasonality does not explain the under-representation in future studies, this underestimate would have important consequences for predictions of climate change, given the strong radiative forcing by N<sub>2</sub>O. If these scaling factors applied uniformly over the USA and Canada, then the yearly anthropogenic contribution of these countries to global emissions would be 49 Tg CH<sub>4</sub> and 4.3 Tg N<sub>2</sub>O. Extending this approach with measurements covering at least one full year would provide valuable information on the

seasonality of emissions. The two main potential sources for bias in this approach, the upwind boundary condition and transport error, could be further quantified and reduced with measured vertical profiles along the boundary, and analysis with gases such as SF<sub>6</sub>, respectively.

## **2.6 Acknowledgments**

Work at AER has been supported by the NASA Terrestrial Ecology Program. EAK acknowledges financial support from the Department of Defense through the NDSEG fellowship program. COBRA-2003 was funded by the NASA Large Scale Biosphere-Atmosphere Experiment in Amazonia (NASA NCC5-590), by NASA support to JBM and BBS (NAG5-11430), and through the NOAA Office of Oceanic and Atmospheric Research. We also thank Ed Dlugokencky and Patricia Lang for analysis and quality control of all CH<sub>4</sub> and N<sub>2</sub>O data.

## **2.7 Supplemental Materials**

### **2.7.1 Sampling Method**

All air samples were collected on board the University of North Dakota Cessna Citation II using the semi-automatic Multiple Enclosure Device for Unfractionated Sampling of Air (MEDUSA). The MEDUSA collects cryogenically dried (-78.5 C dewpoint) air into up to sixteen 1.5 L glass flasks under actively controlled flow and pressure conditions. MEDUSA was designed to sample for laboratory measurements of O<sub>2</sub>/N<sub>2</sub>, Ar/N<sub>2</sub>, δ<sup>13</sup>C(CO<sub>2</sub>), δ<sup>18</sup>O (CO<sub>2</sub>), and CO<sub>2</sub>, but is suitable for other species including CH<sub>4</sub> and N<sub>2</sub>O. The nominal flow rate is 3.3 SLPM, resulting in a 30-second quasi-integrated sample. At a groundspeed of 130 ms<sup>-1</sup>, this corresponds to a horizontal resolution of 4 km and at a climb or descent rate of 10 ms<sup>-1</sup>, this corresponds to a vertical

resolution of 300 m. Each flask has two stopcocks. Flasks intended for the high relative precision measurements of O<sub>2</sub>/N<sub>2</sub> and Ar/N<sub>2</sub> are fitted with viton o-rings, while a subset not used for O<sub>2</sub>/N<sub>2</sub> and Ar/N<sub>2</sub> measurements have teflon o-rings. The flasks are prepared in the laboratory by flushing with cryogenically dried ambient air, and stored with this air inside at 1 atmosphere pressure. In flight, upstream and downstream feedback pressure control loops maintain a constant flow and pressure through the flask. The flasks are purged with over 6 volumes of sample air before sampling. The flow through the flask and the upstream and downstream control pressures were logged at 1 Hz.

The viton o-ring flasks were analyzed at Scripps Institution of Oceanography in a ‘purging mode’ using a ‘push gas’ of known composition (CO<sub>2-push</sub>) to maintain constant pressure and measured for CO<sub>2</sub> (giving CO<sub>2-purge</sub>), O<sub>2</sub>/N<sub>2</sub>, and Ar/N<sub>2</sub>. They were then measured again at Scripps without a push gas giving CO<sub>2-normal</sub>. A dilution value, D, was calculated from the purge-mode (CO<sub>2-purge</sub>), normal-mode (CO<sub>2-normal</sub>), and push gas (CO<sub>2-push</sub>) values according to:

$$D = (\text{CO}_{2\text{-purge}} - \text{CO}_{2\text{-normal}}) / (\text{CO}_{2\text{-purge}} - \text{CO}_{2\text{-push}}) \quad (\text{Equation 2.1})$$

The flasks were then analyzed at NOAA/CMDL (now NOAA/ESRL) for CO<sub>2</sub>, CH<sub>4</sub>, CO, H<sub>2</sub>, N<sub>2</sub>O and SF<sub>6</sub>; and then by University of Colorado Stable Isotope Lab for δ<sup>13</sup>C(CO<sub>2</sub>) and δ<sup>18</sup>O (CO<sub>2</sub>). Because of the use of the push gas, all these measurements were back-corrected for the dilution to derive the ‘true’ value, X<sub>t</sub>:

$$X_t = (X_{\text{meas.}} - X_{\text{push}}(1-D)) / D \quad (\text{Equation 2.2})$$

where X<sub>meas.</sub> and X<sub>push</sub> are the mixing ratio values for the measurement of the mixture of original sample plus push gas, and the push gas, respectively.

The values for the push gas N<sub>2</sub>O, CH<sub>4</sub>, and CO<sub>2</sub> concentration were assigned by CMDL and INSTAAR analyses of prepared flasks. The subset of the flasks with Teflon o-rings were analyzed only at NOAA and the University of Colorado, and thus have D=1. For Scripps flasks, D has a minimum of 0.85, a maximum of 0.91, and a mean of 0.89.

### **2.7.2 WRF runs**

For the runs described in this paper, version 2.2 of the WRF model of Skamarock et al. [2005] was used with a horizontal resolution of 40 km over a domain with corners at 137° W, 5.8° N; 73° W, 5.8° N; 18° W, 58° N; 168° W, 58° N, with initial and boundary conditions provided by the North American Regional Reanalysis [NARR, Mesinger et al., 2006]. A series of 30-hour forecasts was initialized at 00 UTC of each day, from which only hours 6-30 were used to eliminate effects of model spinup; error growth during the 30-hour forecast was limited by nudging the forecast fields to the gridded NARR analysis fields. The WRF model was modified to output hourly averages of mass-coupled advective fields, which were then used within STILT, instead of instantaneous wind fields. This was found to be necessary for satisfactory mass conservation in the STILT computations.

### **2.7.3 Boundary Condition**

The critical aspect of the boundary condition is the variation in space and time of the boundary—offsets do not affect our assessment of surface emissions. For CH<sub>4</sub>, we considered boundary values derived from a run of the TM3 model [Houweling et al., 2006] and also a measurement-derived boundary. Both produce similar results. The data-derived boundary has smaller spatial variation than the TM3 boundary, as we would expect from interpolating sparse data points, and it indicates slightly larger underestimates of sources than the TM3 boundary.

#### 2.7.4 Measurement Uncertainty

There are two major sources of uncertainty present on the measurement axis: atmospheric variability and sampling/instrument error. Atmospheric variability causes variation in measurements that is not captured in the model. We calculated the error from atmospheric variability by assessing the atmospheric variability (“representation error”) in 0.1-hertz CO measurements over an atmospheric correlation length of 170 km [Matross, 2006]. The CO variability was then scaled by a factor taken as the global slope between methane and carbon monoxide over the course of the mission (0.92, this scaling is used throughout when converting CO uncertainty to CH<sub>4</sub> uncertainty). The resulting error for atmospheric variability is 12 nmol/mol (all error numbers in supplemental are 1 $\sigma$ ). The instrument error is taken as 2.0 nmol/mol, based on NOAA lab repeatability. The root sum of squares of these errors results in the use of a total measurement uncertainty  $\pm$  12 nmol/mol.

For nitrous oxide, to find the atmospheric variability we scale the observed CH<sub>4</sub> variability by the nitrous oxide-methane slope in the free troposphere (>3km) of 0.010 as discussed in the main text (this scaling is used throughout when converting from CH<sub>4</sub> uncertainty to N<sub>2</sub>O uncertainty), to get an error of 0.12 nmol/mol. Instrument error is taken as 0.40 nmol/mol, based on NOAA repeatability. The root sum of squares of these errors results in the use of a total measurement uncertainty  $\pm$  0.42 nmol/mol. (Note that if we include an average dilution error factor ( $1/D = 1.12$ ) for the flasks with  $D \neq 1$ , the effect on the retrieved slope is within 1 $\sigma$  uncertainty, i.e. 0.403 to 0.434 for N<sub>2</sub>O EDGAR inventory)

#### 2.7.5 Model Uncertainty

We consider four main components of model uncertainty: boundary condition error, particle statistic error, aggregation error in flux fields, and transport error. For methane, we calculate the boundary condition error by finding the standard deviation of

the difference between model and data above 3km, 19 nmol/mol. This error estimation includes transport error affecting the boundary condition value. Scaled to N<sub>2</sub>O by the slope (0.01), we find an N<sub>2</sub>O boundary error of 0.19 nmol/mol. We take the particle statistic error to be 13% of the enhancement over the advected boundary value, as calculated by Gerbig et al., [2003]. Aggregation error was calculated by Miller et al., [2008] for CO, scaling this number with the slope (0.92) for methane gives 8.7 nmol/mol, and scaling with the slope (0.01) for nitrous oxide gives 0.087 nmol/mol. To estimate transport error, we compared the results derived from WRF fields with results derived from another meteorological product for the first 100 receptor points, the Eta Data Assimilation System 40-km (EDAS) reanalysis fields obtained from the NOAA Air Resources Lab server [Rolph, 1997; <ftp://www.arl.noaa.gov/pub/archives/edas40/>]. The standard deviation of the difference in the two models enhancement signals gives an approximation of transport error on the footprint. These transport errors were found to be 11 nmol/mol for CH<sub>4</sub> and 0.071 nmol/mol for N<sub>2</sub>O. The root sum of squares of these four contributing errors is calculated for each point to determine the model uncertainty.

### **2.7.6 Possible Footprint Bias**

We address variance in footprint strength (via transport error) but have not addressed potential bias in the footprint. Systematic under- or overestimation of the footprint would give corresponding bias in the computed enhancement for the tracer at the receptor. The only way to assess bias in footprint calculations would be to perform an analysis of a gas with known emissions in the region, similarly distributed spatially, but we have no such trace species. But we can consider an ensemble of results for diverse trace species to see if there may exist a consistent bias. We have applied our LPDM also to CO [Miller et. al., 2008], and CO<sub>2</sub> [Matross et. al., 2006]. It was found that that emissions inventories were also significantly low in the case of CO, but notably, these results agree with those found using an entirely different approach with an Eulerian model

and a different meteorological product [Hudman et. al., 2008]. CO<sub>2</sub> results show [Matross et. al., 2006] very close agreement with prior fluxes, and for CO<sub>2</sub> the emissions were derived from actual flux measurements at ecosystem scale. The CO<sub>2</sub> results, held in concert with results presented here, suggest there is not a systematic bias in the footprint calculations. In particular, bias of factors of 2-3 would be inconsistent with well-established principles for light use efficiency of terrestrial vegetation.

### **2.7.7 Considering Uncertainties**

After performing fitxy, we calculate reduced chi-square,  $\chi^2_{\nu}$ , and from that the “ $\chi^2$  probability”, q. In the limit of large n, q=0.5 when  $\chi^2_{\nu}=1$ . For fitting in the CH<sub>4</sub> case, our used uncertainties result in a large q approaching one. Scaling the uncertainties down by a multiplier of (1/1.36) results in a q =0.5. This scaling would reduce the uncertainty in the fit from 7.01% to 4.79%. In the paper we use the more conservative 7.01%, though we appear to have smaller statistical uncertainty. For N<sub>2</sub>O, in both the EDGAR and GEIA case calculated q-values are small. Scaling the uncertainties by 1.18 and 1.142, respectively for EDGAR and GEIA, results in q-values of 0.5. This increases the uncertainty in the slope from 8.03% to 9.50% for EDGAR and from 8.66% to 9.94% for GEIA. The larger uncertainties are used in this work.

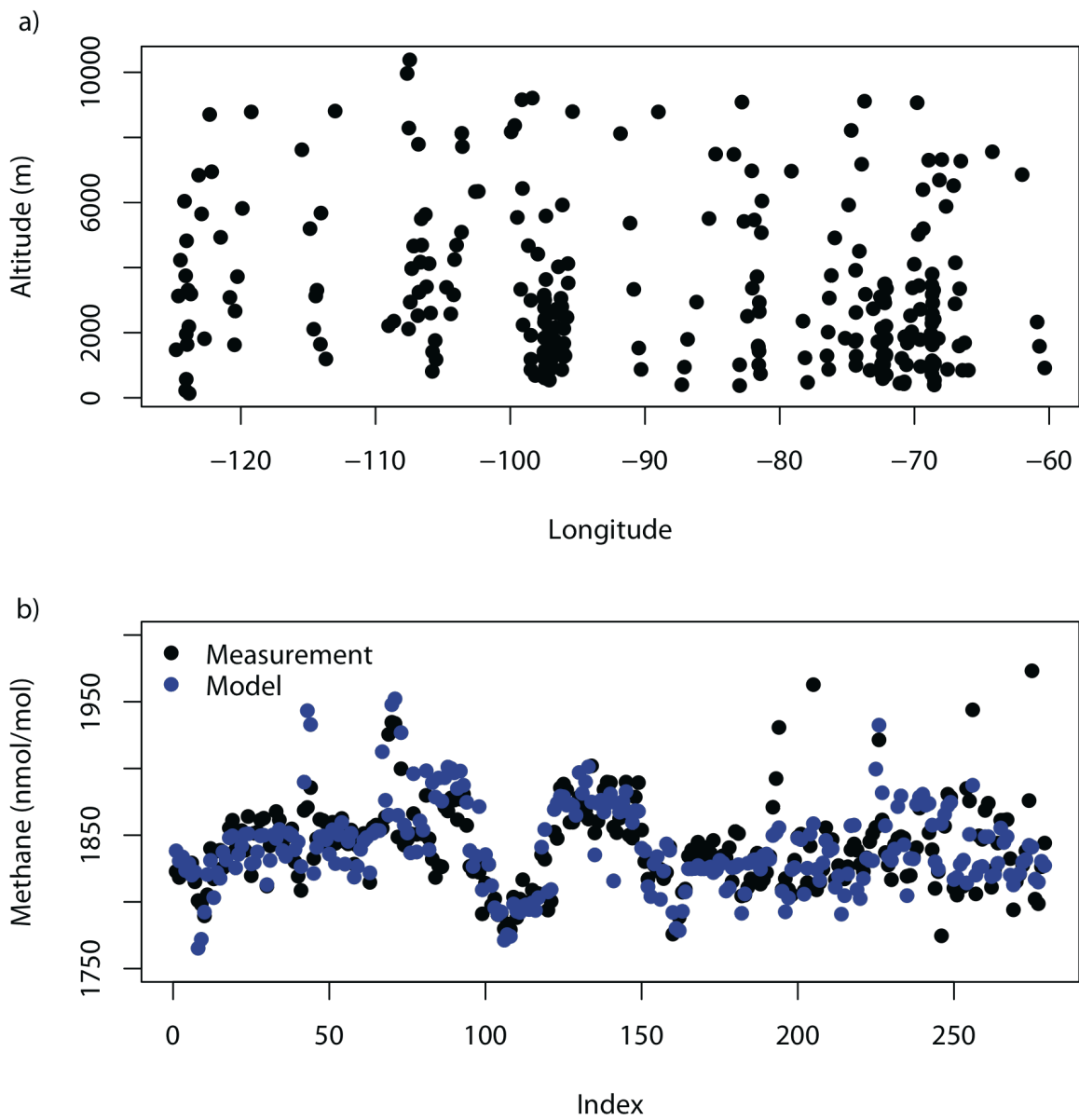


**Figure 2.4** (a) The vertical nature of the sampling. (b) The fidelity of the model to match the observations point by point.

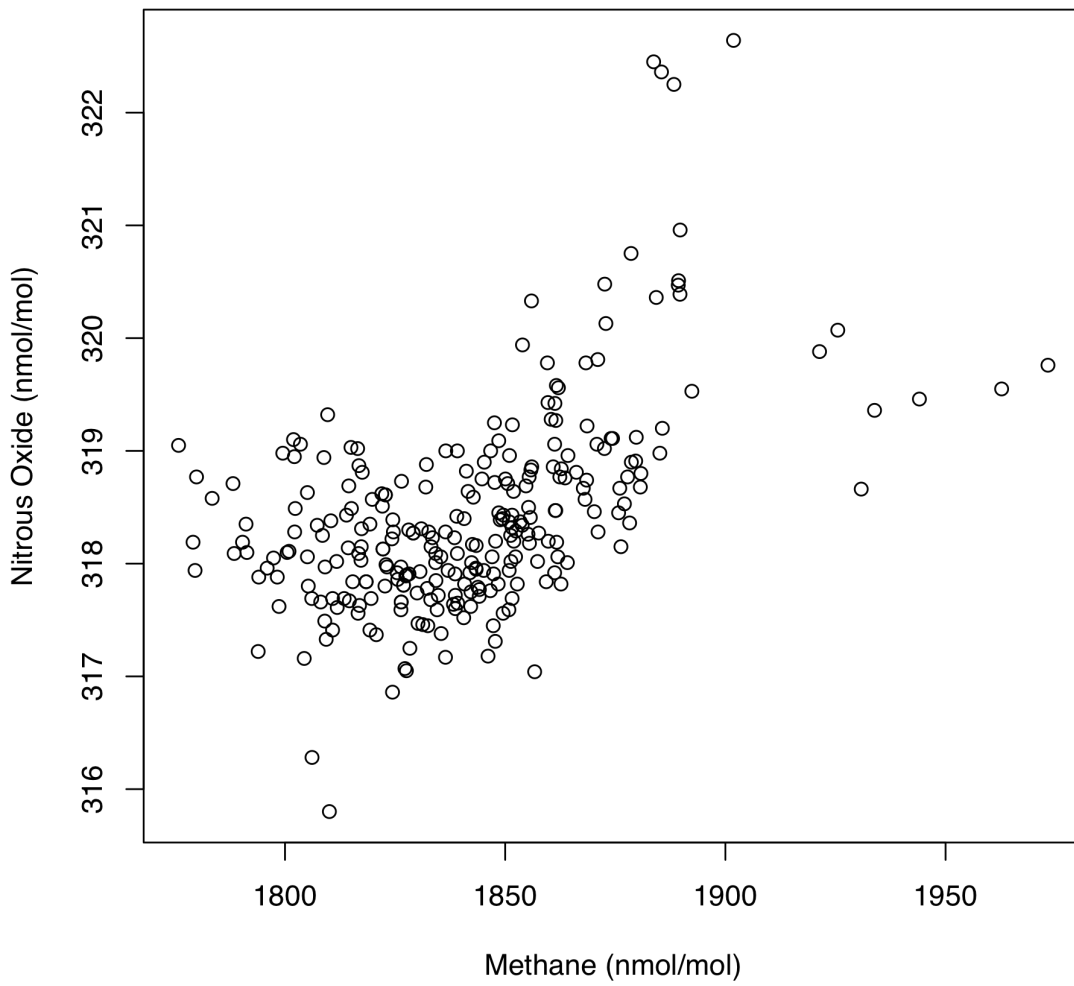


**Figure 2.5** Relationship for all measured points between methane and nitrous oxide.

## References Cited

- Bergamaschi, P., C. Frankenberg, J. F. Meirink, M. Krol, F. Dentener, T. Wagner, U. Platt, J. O. Kaplan, S. Körner, M. Heimann, E. J. Dlugokencky, and A. Goede (2007), Satellite cartography of atmospheric methane from SCIAMACHY on board ENVISAT: 2. Evaluation based on inverse model simulations, *J. Geophys. Res.*, 112, D02304, doi:10.1029/2006JD007268.
- Bouwman, A.F., K.W. van der Hoek and J.G.J. Olivier (1995), Uncertainties in the global source distribution of N<sub>2</sub>O, *J. Geophys. Res.*, 100(D2), 2785-2800.
- Chen, Y.-H., and R. G. Prinn (2006), Estimation of atmospheric methane emissions between 1996 and 2001 using a three dimensional global chemical transport model, *J. Geophys. Res.*, 111, D10307, doi:10.1029/2005JD006058.
- Dlugokencky E. J., R. C. Myers, P. M. Lang, K. A. Masarie, A. M. Croswell, K. W. Thoning, B. D. Hall, J. W. Elkins, L. P. Steele (2005), Conversion of NOAA atmospheric dry air CH<sub>4</sub> mole fractions to a gravimetrically prepared standard scale, *J. Geophys. Res.*, 110, D18306, doi:10.1029/2005JD006035.
- Gerbig, C., J. C. Lin, S. C. Wofsy, B. C. Daube, A. E. Andrews, B. B. Stephens, P. S. Bakwin, and C. A. Grainger (2003), Toward constraining regional-scale fluxes of CO<sub>2</sub> with atmospheric observations over a continent: 2. Analysis of COBRA data using a receptor-oriented framework, *J. Geophys. Res.*, 108(D24), 4757, doi:10.1029/2003JD003770.
- Gimson N.R., and M. Uliasz (2003), The determination of agricultural methane emissions in New Zealand using inverse modeling techniques, *Atmospheric Environment*, 37, 3903-3912.
- Hall B. D., G. S. Dutton, J. W. Elkins (2007), The NOAA nitrous oxide standard scale for atmospheric observations, *J. Geophys. Res.*, 112, D09305, doi:10.1029/2006JD007954.
- Hirsch, A. I., A. M. Michalak, L. M. Bruhwiler, W. Peters, E. J. Dlugokencky, and P. P. Tans (2006), Inverse modeling estimates of the global N<sub>2</sub>O surface flux from 1998–2001, *Global Biogeochem. Cycles*, 20, GB1008, doi:10.1029/2004GB002443.
- Hofmann, D. J., J. H. Butler, E. J. Dlugokencky, J. W. Elkins, K. Masarie, S. A. Montzka, and P. Tans, (2006): The role of carbon dioxide in climate forcing from 1979 - 2004: Introduction of the Annual Greenhouse Gas Index, *Tellus, Ser. B*, 58, 614-619.
- Houweling, S., T. Röckmann, I. Aben, F. Keppler, M. Krol, J. F. Meirink, E. J. Dlugokencky, and C. Frankenberg (2006), Atmospheric constraints on global emissions of methane from plants, *Geophys. Res. Lett.*, 33, L15821, doi:10.1029/2006GL026162.

- Hudman, R.C., L.T. Murray, D. J. Jacob, D.B. Millet, S. Turquety, S. Wu, D. R. Blake, A. H. Goldstein, J. Holloway, G. W. Sachse (2008), Biogenic vs. Anthropogenic sources of CO over the United States, *Geophys. Res. Lett.*, 35, L04801, doi: 10.1029/2007GL032393.
- Hurst, D. F., J. C. Lin, P. A. Romashkin, B. C. Daube, C. Gerbig, D. M. Matross, S. C. Wofsy, B. D. Hall, and J. W. Elkins (2006), Continuing global significance of emissions of Montreal Protocol–restricted halocarbons in the United States and Canada, *J. Geophys. Res.*, 111, D15302, doi:10.1029/2005JD006785.
- Lin, J. C., C. Gerbig, S. C. Wofsy, A. E. Andrews, B. C. Daube, K. J. Davis, and C. A. Grainger (2003), A near-field tool for simulating the upstream influence of atmospheric observations: The Stochastic Time-Inverted Lagrangian Transport (STILT) model, *J. Geophys. Res.*, 108(D16), 4493, doi:10.1029/2002JD003161.
- Matross, D. M. (2006), Regional Scale Land-Atmosphere Carbon Dioxide Exchange: Data Design and Inversion within a Receptor Oriented Modeling Framework, Ph.D. Thesis, Harvard University, Cambridge, MA.
- Matross, D. M., A. Andrews, M. Pathmathevan, C. Gerbig, J. C. Lin, S. C. Wofsy, B. C. Daube, E. W. Gottlieb, V. Y. Chow, J. T. Lee, C. Zhao, P. S. Bakwin, J. W. Munger, and D. Y. Hollinger (2006), Estimating regional carbon exchange in New England and Quebec by combining atmospheric, ground-based and satellite data, *Tellus, Ser. B*, 58, 344-358.
- Mesinger, F., G. DiMego, E. Kalnay, K. Mitchell, P. C. Shafran, W. Ebisuzaki, D. Jovic, J. Woollen, E. Rogers, E. H. Berbery, M. B. Ek, Y. Fan, R. Grumbine, W. Higgins, H. Li, Y. Lin, G. Manikin, D. Parrish, and W. Shi (2006), North American Regional Reanalysis, *Bull. Amer. Meteor. Soc.*, 87 (3), 343-360.
- Miller, J. B., and P. P. Tans (2003), Calculating isotopic fractionation from atmospheric measurements at various scales, *Tellus, Ser. B*, 55(2), 207-214.
- Miller, J. B., L.V. Gatti, M.T.S. d'Amelio, A.M. Crotwell, E.J. Dlugokencky, P. Bakwin, P. Artaxo, and P.P. Tans (2007), Airborne sampling reveals large methane enhancement over the Amazon basin, *Geophys. Res. Lett.*, 34, L10809, doi:10.1029/2006GL029213.
- Miller, S. M., D. M. Matross, A. E. Andrews, D. B. Millet, M. Longo, E. W. Gottlieb, A. I. Hirsch, C. Gerbig, J. C. Lin, B. C. Daube, R. C. Hudman, P. L. S. Dias, V. Y. Chow, and S. C. Wofsy (2008), Sources of carbon monoxide and formaldehyde in North America determined from high-resolution atmospheric data, *Atmos. Chem. Phys. Discuss.*, 8, 11395-11451.
- Nevison, C.D., N.M. Mahowald, R.F. Weiss, and R.G. Prinn (2007), Interannual and seasonal variability in atmospheric N<sub>2</sub>O, *Global Biogeochem. Cycles*, 21, GB3017, doi:10.1029/2006GB002755.

- Olivier, J.G.J., Van Aardenne, J.A., Dentener, F., Ganzeveld, L. and J.A.H.W. Peters (2005), Recent trends in global greenhouse gas emissions: regional trends and spatial distribution of key sources. In: “Non-CO2 Greenhouse Gases (NCGG-4)”, A. van Amstel (coord.), page 325-330. Millpress, Rotterdam, ISBN 90 5966043 9.
- Press, W.H., S.A. Teukolsky, W.T. Vetterling, and B.P. Flannery (1992), Numerical Recipes in FORTRAN The Art of Scientific Computing, 2nd ed., Cambridge Univ. Press, New York.
- Prinn, R., D. Cunnold, R. Rasmussen, P. Simmonds, F. Alyea, A. Crawford, P. Fraser, and R. Rosen (1990), Atmospheric emissions and trends of nitrous oxide deduced from 10 years of ALE-GAGE data, *J. Geophys. Res.*, 95(D11), 18,369– 18,385.
- Rolph, G. D. NOAA NCEP Eta Data Assimilation System (EDAS) archived by NOAA Air Resources Laboratory (The EDAS Archive). U.S. Department of Commerce, NOAA Air Resources Laboratory (ARL). 1997
- Skamarock, W. C., J. B. Klemp, J. Dudhia, D. O. Gill, D. M. Barker, W. Wang, and J. G. Powers (2005), A description of the advanced research WRF version 2. Technical Note 468+STR, MMM Division, NCAR, Boulder, CO, 88 pp. Available from [http://www.mmm.ucar.edu/wrf/users/docs/arw\\_v2.pdf](http://www.mmm.ucar.edu/wrf/users/docs/arw_v2.pdf)
- Stohl, A., C. Forster, S. Eckhardt, N. Spichtinger, H. Huntrieser, J. Heland, H. Schlager, S. Wilhelm, F. Arnold, and O. Cooper (2003), A backward modeling study of intercontinental pollution transport using aircraft measurements, *J. Geophys. Res.*, 108(D12), 4370, doi:10.1029/2002JD002862.

## CHAPTER 3

### **Atmospheric constraints on 2004 emissions of methane and nitrous oxide in North America from atmospheric measurements and a receptor-oriented modelling framework**

[Kort, E. A., A. E. Andrews, E. Dlugokencky, C. Sweeney, A. Hirsch, J. Eluszkiewicz, T. Nehrkorn, A. Michalak, B. Stephens, C. Gerbig, J. B. Miller, J. Kaplan, S. Houweling, B. C. Daube, B. C. Daube, P. Tans, and S. C. Wofsy (2010), Atmospheric constraints on 2004 emissions of methane and nitrous oxide in North America from atmospheric measurements and a receptor-oriented modeling framework, *Journal of Integrative Environmental Sciences*, 7:2, 125-133, doi:10.1080/19438151003767483.

#### **Abstract**

Methane and nitrous oxide are potent greenhouse gases whose atmospheric abundances have increased significantly in the past 200 years, together accounting for approximately half of the radiative forcing associated with increasing concentrations of carbon dioxide. In order to understand the factors causing increases of these gases globally, we need to determine their emission rates at regional to continental scales. We directly link atmospheric observations with surface emissions using a Lagrangian Particle Dispersion Model, and then determine emission rates by optimizing prior emissions estimates. We use measurements from NOAA's tall tower and aircraft program in 2004, The Stochastic Time-Inverted Lagrangian Transport model (STILT) driven by meteorological fields from a customized version of the Weather Research and Forecasting (WRF) model, and EDGAR32FT2000 and GEIA as prior emission estimates. In the US and Canada, methane emission rates are found to be consistent with observations, while nitrous oxide emissions are significantly low, by a factor 2.5-3 in the peak emissions time period found to be February through May.

### **3.1 Introduction**

In the current environment of rising greenhouse gas concentrations and potential resultant consequences, atmospheric evidence of emissions of these gases is crucial in understanding their impact on current and future climate and guiding relevant policy. Though much attention has focused on carbon dioxide as the single most important anthropogenic greenhouse gas [Hofmann et al., 2006], non-CO<sub>2</sub> greenhouse gases play a significant role in the Earth's energy balance. Non-CO<sub>2</sub> greenhouse gases contribute a comparable amount to radiative forcing as carbon dioxide [Hofmann et al., 2006], with methane and nitrous oxide as the first and second (<http://www.esrl.noaa.gov/gmd/aggi/>) largest contributors respectively.

Many global-scale studies have investigated emissions of methane and nitrous oxide (Bergamaschi et al., 2007; Chen and Prinn, 2006; Houweling et al., 2006; Huang et al., 2008; Nevison et al., 2007; Hirsch et al., 2006; Prinn et al., 1990). These studies help immensely to improve understanding of emissions at large spatial and temporal scales (continental and annual). Studies on a more focused spatial and temporal scale, such as taken in Miller et al. (2007), have been more limited. Recent work (Kort et al., 2008) examining U.S. and Canadian emissions in Spring 2003 indicated methane emissions were consistent with predictions (49 Tg CH<sub>4</sub>/yr), while nitrous oxide emissions were 2.5-3 times higher than predicted by EDGAR or GEIA. These results leave open questions about seasonal variation and annual total emissions of nitrous oxide and methane. Are nitrous oxide emissions two to three times larger than expected for the full calendar year? In this work we target these questions by examining measurements collected in 2004 from aircraft and towers. By focusing on areas adjacent to particular receptor sites, our analysis provides a preliminary assessment for the application of these types of observations for verification of reported emissions at regional scales.

### **3.2 Measurements**

Flask samples collected in 2004 from aircraft performing vertical profiling and from tall towers were used in this study. All flasks were analyzed at NOAA/ESRL for CO<sub>2</sub>, CO, CH<sub>4</sub>, H<sub>2</sub>, SF<sub>6</sub>, and N<sub>2</sub>O dry air mole fractions. Methane and nitrous oxide measurements used here are calibrated on the NOAA2004 (Dlugokencky et al., 2005) and NOAA2006 (Hall et al., 2007) scales, respectively. Vertical profiling measurements used in the methane analysis were collected at three sites representing different regions of North America: a remote plain site in Briggsdale, Colorado (CAR, 40.37° N, -104.30° W, 2000-8000 masl), a remote forested site in Park Falls, Wisconsin (LEF, 45.93° N, -90.27° W, 500-4000 masl), and a more urban site in Worcester, Massachusetts (NHA, 42.95° N, -70.63° W, 500-7000 masl). Tall tower measurements used in the nitrous oxide analyses were collected at the LEF site (45.93° N, -90.27° W, 472 masl). Climatologically, 2004 was wetter than average in the Southern and Eastern US, though the Western US had a continuation of a multi-year drought. The Northeast and Central US up into Central Canada had much colder than average summers.

### **3.3 Methodology**

The analysis approach here closely follows prior work outlined in Kort et al. (2008). The scheme represents the application of a ‘top-down’ method as a check on ‘bottom-up’ inventories. Measurements and prior emissions estimates are linked together in a regional modeling framework built upon a Lagrangian Particle Dispersion Model (LPDM), the Stochastic Time-Inverted Lagrangian Transport model (STILT) (Lin et al., 2003). With this technique we can predict mixing ratios of specific gases at the time and location of a measurement based upon prior emissions estimates. This facilitates direct comparison and assessment of the accuracy of the prior flux estimates.

#### **3.3.1 Meteorological Input**

We drive STILT with meteorological fields from the Weather Research and

Forecasting (WRF) model (Skamarock et al., 2005). WRF is run in the same customized manner as described in Kort et al. (2008), ensuring mass conservation, with the addition of a nested 10-km domain within the larger 40-km domain.

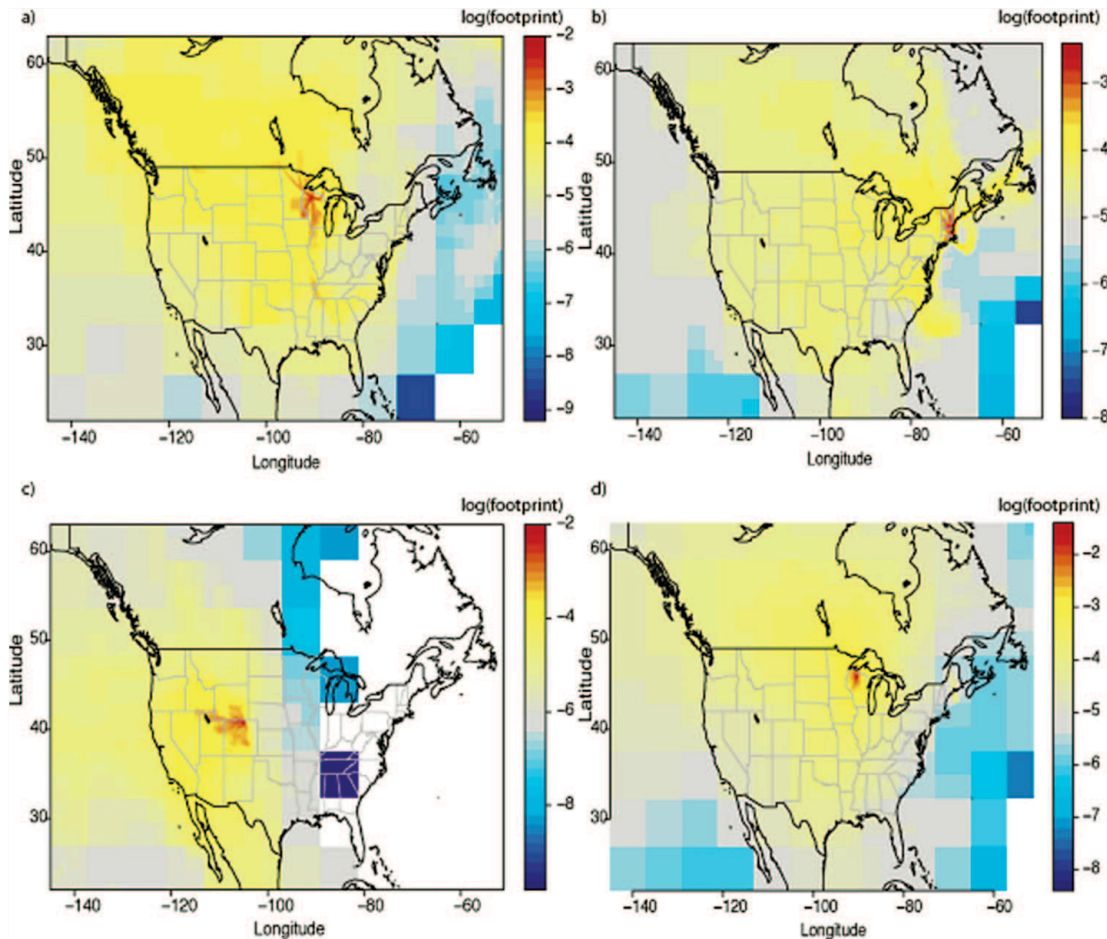


**Figure 3.1** Average footprint of aircraft measurements (a) at LEF (b) at NHA (c) at CAR (d) of measurements made at the tall tower at LEF. Dynamic resolution is used in plotting, with grid boxes increasing in size at greater distances from receptor origin.

### 3.3.2 Footprint Estimation, Emissions Inventories, and Upwind Boundary Condition

Using the WRF fields, STILT transports ensembles of 500 particles backwards in time for 10 days for each point in space and time where flask samples were collected (receptor point). From these trajectories, we calculate a footprint for each receptor point

representing the sensitivity of the receptor point to surface fluxes, in units of  $\text{ppb}/(\mu\text{mol m}^{-2} \text{ s}^{-1})$ . Average footprints for the four measurement locations are visualized in figure 3.1. Multiplying the footprint by a prior flux field gives the enhancement predicted at the receptor point due to the estimated fluxes. Addition of this value to a boundary condition term, derived by assigning a mixing ratio to a particle as it crosses  $-145^\circ \text{ W}$ , allows for direct comparison between modelled and measured values. Prior flux fields used here are EDGAR 32FT2000 (Olivier et al., 2005) with the ‘JK’ wetland inventory (Bergamaschi et al., 2007) for  $\text{CH}_4$  and EDGAR 32FT2000 and GEIA (Bouwman et al., 1995) for  $\text{N}_2\text{O}$  (as described in more detail in Kort et al., 2008). For  $\text{N}_2\text{O}$ , GEIA includes both natural and anthropogenic sources, while EDGAR only includes anthropogenic. Boundary condition values used here are derived from interpolation between data collected over the Pacific for methane, as done by Gerbig et al. (2003) for  $\text{CO}$  and  $\text{CO}_2$ , and by temporal interpolation of free tropospheric values measured in aircraft profiles above LEF for nitrous oxide. For nitrous oxide this boundary approach should account for larger scale stratospheric influence on tropospheric  $\text{N}_2\text{O}$  mixing ratios, and stratospheric influence not captured here would translate to model results over-predicting mixing ratios, and therefore underestimating sources.

### 3.3.3 Optimization Approach

In assessment of methane emissions, we follow the same optimization approach outlined in Kort et al. (2008). For both LEF and NHA, we apply a  $\chi^2$  fit (fitexy) between modelled and measured values including uncertainties in both  $x$  and  $y$  (Press et al., 1992). We find one scaling factor, the inverse of the fit slope, for the entire emissions field. This approach assumes constant errors in the prior emissions field and finds different scaling factors for the different sites; each nominally applies to the entire emissions field, but in fact applies only to the small regions defined by the footprint (figure 3.1). Uncertainties in the scaling factor are directly retrieved from the  $\chi^2$  fit, and are defined by the

uncertainties included in the fitting (measurement error, model-data mismatch, boundary condition error, particle statistic error, aggregation error in flux fields, and transport error, as defined in Kort et al., 2008). This approach offers a simple one-parameter optimization insensitive to constant biases in the advected boundary condition. It assumes that the slope is driven by emissions, not boundary variation, and that error in the spatial distribution of the prior emissions fields do not contribute.

### **3.4 Results: Methane**

#### **3.4.1 Briggsdale, Colorado (CAR)**

Profiles at CAR see weaker upwind emissions that are well mixed vertically, only occasionally encountering plumes influenced by large local sources such as natural gas extraction sites. The vertical profile shows little variation with altitude (figure 3.2b), and the measured vs. modelled graph predominantly shows point-to-point scatter representative of error in the advected boundary condition (figure 3.2a). The absence of a strong source signature renders the fit-optimization method moot, as model and measurements mostly agree and most points have little or no surface emission influence; thus no optimization is attempted at CAR.

#### **3.4.2 Park Falls, Wisconsin (LEF)**

Measurements at LEF show a significant signature of sources, as seen in the strong vertical gradient (figure 3.2d). Seasonality in the methane values is seen due to variations in the latitudinal origins of the air mass seen at LEF, and the seasonal variation of the upwind boundary condition (largely due to OH). Fitting the model vs. measurement, using the same uncertainty approach as in Kort et al. (2008), finds a slope of  $0.76 \pm 0.15$  (2-sigma), which converts to a scaling factor of  $1.3 \pm 0.3$ .

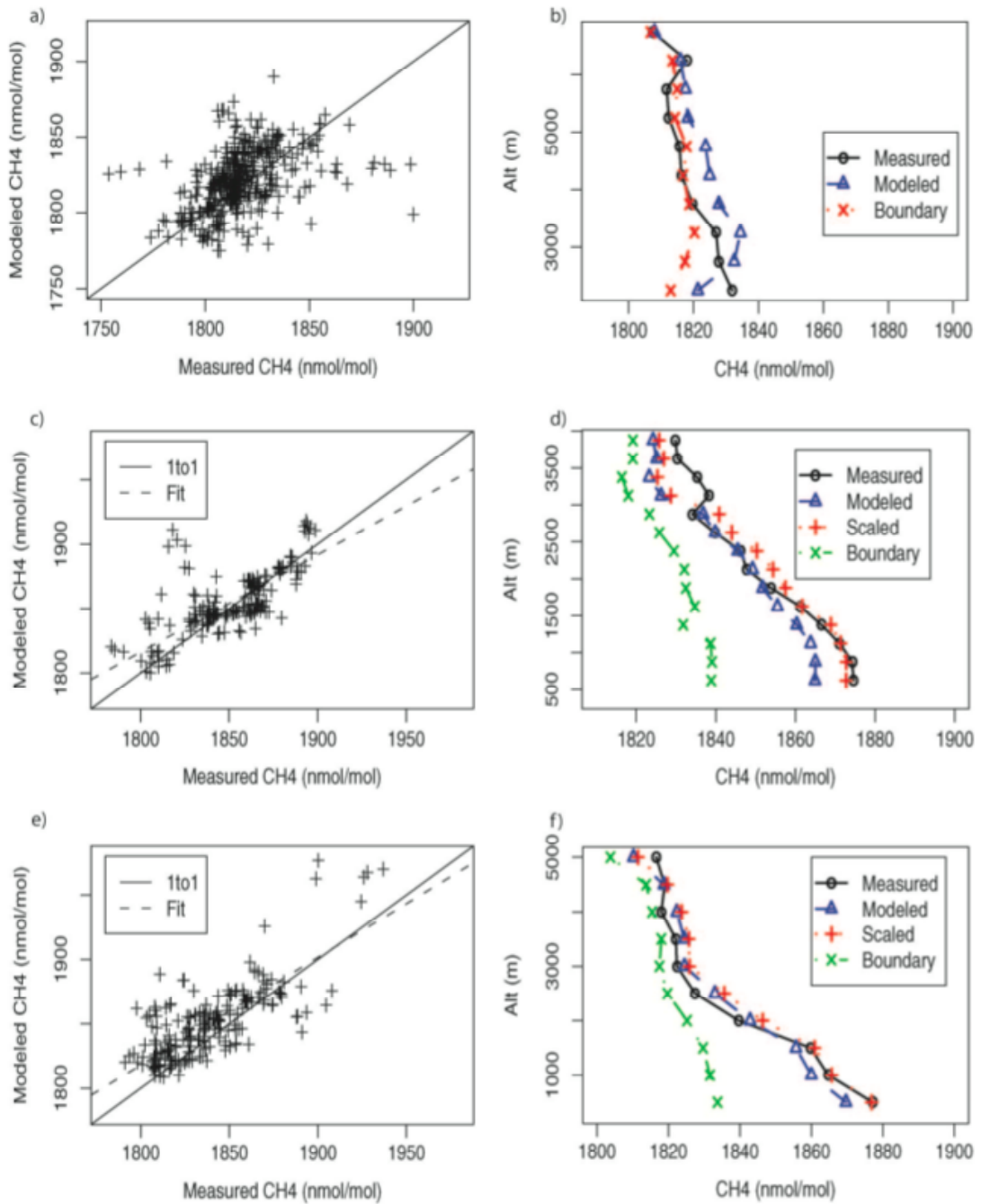


**Figure 3.2** (a) Comparison of measured and modeled values at CAR with 1 to 1 line. (b) Average, binned vertical profile at CAR. (c) Modeled vs. Measured with fit at LEF. (d) Average, binned vertical profile at LEF. (e) Modeled vs. measured with fit at NHA. (f) Average, binned vertical profile at NHA.

### **3.4.3 Worcester, Massachusetts (NHA)**

At NHA enhancement in the boundary layer due to regional emissions also presents itself as a strong vertical gradient (figure 3.2f). Again seasonality lies not within the sources, so much as in the origins in the air mass seen at NHA. Fitting model vs. measurement for NHA finds a slope of  $0.84 \pm 0.14$ , which converts to a scaling factor of  $1.2 \pm 0.2$ .

### **3.4.4 Boundary Condition**

Due to seasonal changes and a large latitudinal gradient, the upwind boundary conditions appears to be biased based on a comparison between model and measured mixing ratios in the free troposphere at NHA and LEF. At NHA a bias of 13 ppb is found by considering all modelled and measured data above 3km, and this bias is removed from the boundary condition in plotting figure 3.2f. At LEF, much sparser free troposphere data is available, so the full column average is considered, retrieving a bias of 9 ppb between measured and scaled-modelled columns, and this bias is removed from the boundary condition in plotting figure 3.2d. Because our analysis is focused on the scaling factor, or slope, between modelled and measured data the bias, or intercept, is not critical to our analysis. Nevertheless, the variability in the bias between stations would add significant uncertainty to inverse analysis where observations at multiple sites were used to estimate fluxes from specific regions.

### **3.4.5 Source Partitioning**

Figure 3.3 illustrates the contributions of different source categories (as defined in EDGAR + wetlands) at LEF and NHA according to model results (note the retrieved scaling factor is applied uniformly to all EDGAR categories). Strong regional sources of fossil fuel use, agriculture, and waste handling (EDGAR categories) produce the majority of the enhancement in the boundary layer at both LEF and NHA. We are not primarily

detecting natural sources with these measurements; instead we are constraining anthropogenic sources. We cannot distinguish these purely from the measurements, but instead rely on the model to partition sources. The agreement between model and measurement suggest the prior emissions fields accurately distribute and partition the different methane sources. Fire emissions are not included in the analysis, as very few flasks considered were strongly influenced by biomass burning, as indicated by CO values generally being less than 200 ppb.

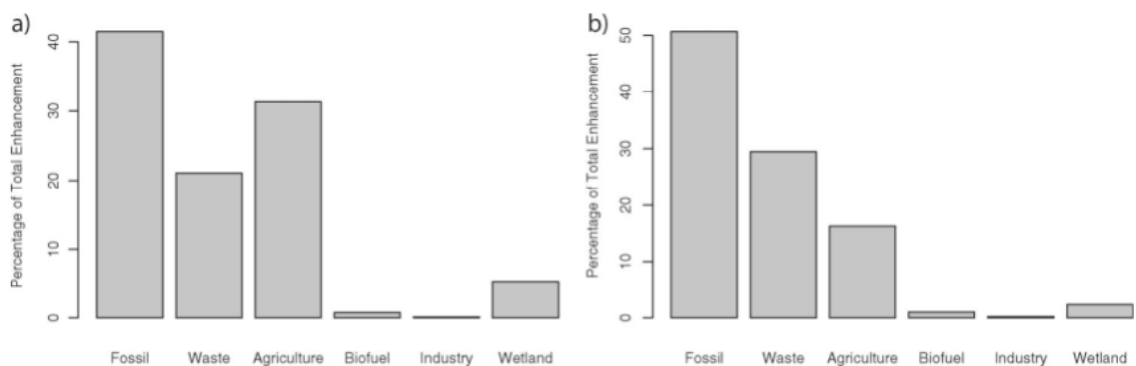


**Figure 3.3** Percentage contribution of different source categories in the model (a) at LEF. (b) at NHA.

### 3.5 Results: Nitrous Oxide

LEF lies in close proximity to large agricultural lands, advantageous in assessing seasonality of nitrous oxide emissions. Prior emissions from both EDGAR and GEIA are considered. Resulting time series can be seen in figure 3.4. For both EDGAR and GEIA, model and measurements closely agree for summer, fall, and early winter, but late winter and spring show large deviations between model and measurements. R-squared values for the model results are 0.34 and 0.25 respectively for EDGAR and GEIA. By applying the scaling factors found during spring in Kort et al. 2008 (2.62 & 3.05 for EDGAR and GEIA) to just the late winter and spring months (February through May), the agreement improves dramatically, resulting in r-squared values of 0.59 and 0.50. Application of this



scaling factor for the full year, or different time windows worsens model-data agreement. This temporal application of the scaling is mostly consistent with the enhanced emissions being agriculturally related: flux measurements at an agricultural site in Ontario, Canada (similar latitude to LEF) find nitrous oxide emissions peaks occurring roughly in this same time domain (Wagner-Riddle et al., 2007).

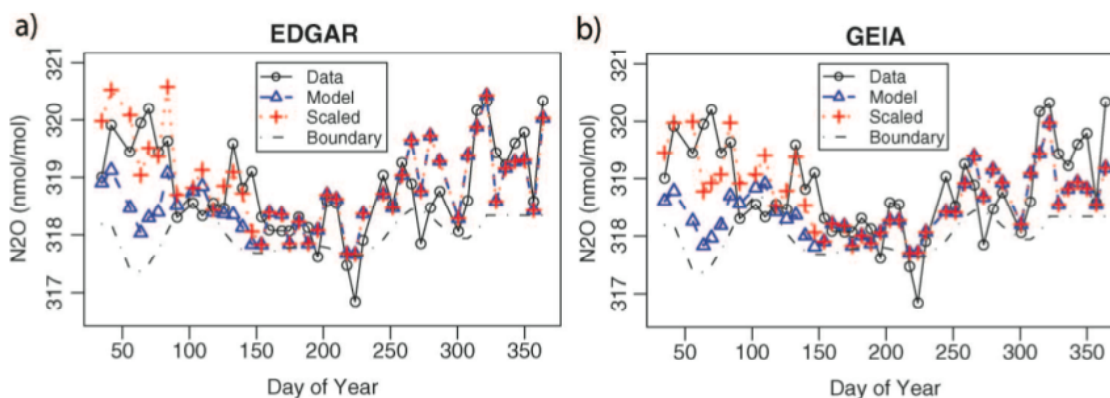


**Figure 3.4** (a) Time series of measurements (black circle), boundary condition (black dashed), prior model with EDGAR (blue triangle), and the model scaled in late winter and spring (red cross). (b) same as (a), except the emissions model is GEIA.

### 3.6 Conclusion

Findings here expand upon prior work analyzing COBRA-NA data from the spring of 2003. Consideration of a full calendar year indicates that prior methane emissions estimates from EDGAR32FT2000 are consistent with observations, as found in Kort et al. (2008). We did note scaling factors of 1.2 and 1.3, indicating emissions could be somewhat higher, but these scaling factors are of marginal statistical significance as they fall at the limit of what can be resolved with current data sets and techniques. Other regional top-down studies in the US have either found EDGAR32FT2000 emissions to be consistent or low (Zhao et. al., 2009; Wunch et. al., 2009). The recently released EDGAR v4.0 (European Commission, Joint Research Centre (JRC)/Netherlands Environmental Assessment Agency (PBL). Emission Database for Global Atmospheric

Research (EDGAR), release version 4.0. <http://edgar.jrc.ec.europa.eu>, 2009) reduces US anthropogenic emissions by 30%, and this reduction is neither consistent with this nor prior studies.

Nitrous oxide findings support the view that high emission rates derived for spring from COBRA-NA reflect seasonality of the emissions, with strongest emissions in

late winter and early spring. We estimate total U.S. and Canadian anthropogenic nitrous oxide emissions to be larger than EDGAR's 1.6 Tg N<sub>2</sub>O/yr by  $0.9 \pm 0.2$  Tg N<sub>2</sub>O/yr, summing to  $\sim 2.5$  Tg N<sub>2</sub>O/yr, with 1.4 Tg emitted over the 4 month peak (February through May) and 1.1 Tg emitted over the remaining 8 months. Considering global emissions as reported by the IPCC (Denman et. al., 2007), these emissions would represent 9% of the total global N<sub>2</sub>O source, and 24% of the anthropogenic source.

By focusing on relatively small areas ( $10^4$ - $10^5$  km<sup>2</sup>) representing the flux-weighted footprint, this work provides a preliminary assessment for using atmospheric observations to verify reported emissions. Using currently available data we can resolve discrepancies in methane emissions larger than 20-30% on a regional scale. Limitations include: potential bias in footprint strength, varying boundary condition bias with altitude, and the influence of errors in the assumed spatial distribution of emissions. The latter two problems can be addressed by denser spacing of aircraft data, satellite data to help define the boundary condition, and the application of more sophisticated inversions to reduce reliance on prior emissions fields (Meirink et. al., 2008; Michalak et. al., 2004).

### 3.7 Acknowledgments

Support for this work has come from NASA through both the MAP project (NNX07AU33G) and the Non-CO<sub>2</sub> synthesis project (NNX08AR47G) as well as from NSF project ATM-0830916. Computing for this project has made use of NASA HEC resources. We would like to thank Patricia Lang and Kelly Sours for NOAA air sample analysis. EAK acknowledges financial support from the Department of Defense through

the NDSEG fellowship program. We also thank Dan Baumann and Ron Teclaw for sample collection at LEF.

## References Cited

- Bergamaschi, P., C. Frankenberg, J. F. Meirink, M. Krol, F. Dentener, T. Wagner, U. Platt, J. O. Kaplan, S. Körner, M. Heimann, E. J. Dlugokencky, and A. Goede (2007), Satellite cartography of atmospheric methane from SCIAMACHY on board ENVISAT: 2. Evaluation based on inverse model simulations, *J. Geophys. Res.*, 112, D02304, doi:10.1029/2006JD007268.
- Bouwman, A.F., K.W. van der Hoek and J.G.J. Olivier (1995), Uncertainties in the global source distribution of N<sub>2</sub>O, *J. Geophys. Res.*, 100(D2), 2785-2800.
- Chen, Y.-H., and R. G. Prinn (2006), Estimation of atmospheric methane emissions between 1996 and 2001 using a three dimensional global chemical transport model, *J. Geophys. Res.*, 111, D10307, doi:10.1029/2005JD006058.
- Denman, K.L., G. Brasseur, A. Chidthaisong, P. Ciais, P.M. Cox, R.E. Dickinson, D. Hauglustaine, C. Heinze, E. Holland, D. Jacob, U. Lohmann, S. Ramachandran, P.L. de Silva Dias, S.C. Wofsy, and X. Zhang, 2007: Couplings Between Changes in the Climate System and Biogeochemistry. In: *Climate Change 2007: The Physical Science Basis. Contribution of Working Group I to the Fourth Assessment Report of the Intergovernmental Panel on Climate Change* [Solomon, S., D. Qin, M. Manning, Z. Chen, M. Marquis, K.B. Averyt, M. Tignor and H.L. Miller (eds.)]. Cambridge University Press, Cambridge, United Kingdom and New York, NY, USA.
- Dlugokencky E. J., R. C. Myers, P. M. Lang, K. A. Masarie, A. M. Crotwell, K. W. Thoning, B. D. Hall, J. W. Elkins, L. P. Steele (2005), Conversion of NOAA atmospheric dry air CH<sub>4</sub> mole fractions to a gravimetrically prepared standard scale, *J. Geophys. Res.*, 110, D18306, doi:10.1029/2005JD006035.
- Gerbig, C., J. C. Lin, S. C. Wofsy, B. C. Daube, A. E. Andrews, B. B. Stephens, P. S. Bakwin, and C. A. Grainger (2003), Toward constraining regional-scale fluxes of CO<sub>2</sub> with atmospheric observations over a continent: 1. Observed spatial variability from airborne platforms, *J. Geophys. Res.*, 108(D24), 4757, doi:10.1029/2003JD003770.
- Hall B. D., G. S. Dutton, J. W. Elkins (2007), The NOAA nitrous oxide standard scale for atmospheric observations, *J. Geophys. Res.*, 112, D09305, doi:10.1029/2006JD007954.
- Hirsch, A. I., A. M. Michalak, L. M. Bruhwiler, W. Peters, E. J. Dlugokencky, and P. P. Tans (2006), Inverse modeling estimates of the global N<sub>2</sub>O surface flux from 1998–2001, *Global Biogeochem. Cycles*, 20, GB1008, doi:10.1029/2004GB002443.
- Hofmann, D. J., J. H. Butler, E. J. Dlugokencky, J. W. Elkins, K. Masarie, S. A. Montzka, and P. Tans, (2006): The role of carbon dioxide in climate forcing from 1979 - 2004: Introduction of the Annual Greenhouse Gas Index, *Tellus, Ser. B*, 58, 614-619.

- Houweling, S., T. Röckmann, I. Aben, F. Keppler, M. Krol, J. F. Meirink, E. J. Dlugokencky, and C. Frankenberg (2006), Atmospheric constraints on global emissions of methane from plants, *Geophys. Res. Lett.*, 33, L15821, doi:10.1029/2006GL026162.
- Huang, J., A. Golombek, R. Prinn, R. Weiss, P. Fraser, P. Simmonds, E.J. Dlugokencky, B. Hall, J. Elkins, P. Steele, R. Langenfels, P. Krummel, G. Dutton, and L. Porter (2008), Estimation of regional emissions of nitrous oxide from 1997 to 2005 using multinetwerk measurements, a chemical transport model, and an inverse method, *J. Geophys. Res.*, 113, D17313, doi:10.1029/2005JD006785.
- Hurst, D. F., J. C. Lin, P. A. Romashkin, B. C. Daube, C. Gerbig, D. M. Matross, S. C. Wofsy, B. D. Hall, and J. W. Elkins (2006), Continuing global significance of emissions of Montreal Protocol–restricted halocarbons in the United States and Canada, *J. Geophys. Res.*, 111, D15302, doi:10.1029/2005JD006785.
- Kort, E. A., J. Eluszkiewicz, B. B. Stephens, J. B. Miller, C. Gerbig, T. Nehr Korn, B. C. Daube, J. O. Kaplan, S. Houweling, and S. C. Wofsy (2008), Emissions of CH<sub>4</sub> and N<sub>2</sub>O over the United States and Canada based on a receptor-oriented modeling framework and COBRA-NA atmospheric observations, *Geophys. Res. Lett.*, 35, L18808, doi:10.1029/2008GL034031.
- Lin, J. C., C. Gerbig, S. C. Wofsy, A. E. Andrews, B. C. Daube, K. J. Davis, and C. A. Grainger (2003), A near-field tool for simulating the upstream influence of atmospheric observations: The Stochastic Time-Inverted Lagrangian Transport (STILT) model, *J. Geophys. Res.*, 108(D16), 4493, doi:10.1029/2002JD003161.
- Meirink, J. F., P. Bergamaschi, M. C. Krol (2008), Four-dimensional variational data assimilation for inverse modeling of atmospheric methane emissions: method and comparison with synthesis inversion, *Atmospheric Chemistry and Physics*, 8, 21, 6341-6353
- Michalak A. M., L. Bruhwiler, P. P. Tans (2004), A geostatistical approach to surface flux estimation of atmospheric trace gases, *J. Geophys. Res.*, 109(D14), doi: 10.1029/2003JD004422
- Miller, J. B., L.V. Gatti, M.T.S. d’Amelio, A.M. Crotwell, E.J. Dlugokencky, P. Bakwin, P. Artaxo, and P.P. Tans (2007), Airborne sampling reveals large methane enhancement over the Amazon basin, *Geophys. Res. Lett.*, 34, L10809, doi:10.1029/2006GL029213.
- Nevison, C.D., N.M. Mahowald, R.F. Weiss, and R.G. Prinn (2007), Interannual and seasonal variability in atmospheric N<sub>2</sub>O, *Global Biogeochem. Cycles*, 21, GB3017, doi:10.1029/2006GB002755.
- Olivier, J.G.J., Van Aardenne, J.A., Dentener, F., Ganzeveld, L. and J.A.H.W. Peters (2005), Recent trends in global greenhouse gas emissions: regional trends and spatial distribution of key sources. In: “Non-CO<sub>2</sub> Greenhouse Gases (NCGG-4)”, A. van Amstel (coord.), page 325-330. Millpress, Rotterdam, ISBN 90 5966043 9.

- Press, W. H., S. A. Teukolsky, W. T. Vetterling, and B. P. Flannery (1992), *Numerical Recipes in FORTRAN: The Art of Scientific Computing*, 2nd ed., Cambridge Univ. Press, New York.
- Prinn, R., D. Cunnold, R. Rasmussen, P. Simmonds, F. Alyea, A. Crawford, P. Fraser, and R. Rosen (1990), Atmospheric emissions and trends of nitrous oxide deduced from 10 years of ALE-GAGE data, *J. Geophys. Res.*, 95(D11), 18,369– 18,385.
- Skamarock, W. C., J. B. Klemp, J. Dudhia, D. O. Gill, D. M. Barker, W. Wang, and J. G. Powers (2005), A description of the advanced research WRF version 2. Technical Note 468+STR, MMM Division, NCAR, Boulder, CO, 88 pp. Available from [http://www.mmm.ucar.edu/wrf/users/docs/arw\\_v2.pdf](http://www.mmm.ucar.edu/wrf/users/docs/arw_v2.pdf)
- Wagner-Riddle C., A. Furon, N. L. McLaughlin, I. Lee, J. Barbeau, S. Jayasundara, G. Parkin, P. von Bertoldi, and J. Warland (2007), Intensive measurement on nitrous oxide emissions from a corn-soybean-wheat rotation under two contrasting management systems over 5 years, *Global Change Biology*, 13, 1722-1736, doi: 10.1111/j.1365-2486.2007.01388.x
- Wunch D., P.O. Wennberg, G.C. Toon, G Keppel-Aleks, Y.G. Yavin (2009), Emissions of greenhouse gases from a North American megacity, *Geophys. Res. Lett.*, 36, L15810, doi:10.1029/2009GL039825.
- Zhao C.F., A.E. Andrews, L. Bianco, J. Eluszkiewicz, A. Hirsch, C. MacDonald, T. Nehr Korn, M.L. Fischer (2009), *J. Geophys. Res.*, 114(D16302), doi: 10.1029/2008JD011671.

## **CHAPTER 4**

### **Instrumentation: Airborne Observations of Carbon Dioxide, Carbon Monoxide, Methane, and Nitrous Oxide**

#### **Abstract**

A new instrument for airborne measurements of carbon dioxide (CO<sub>2</sub>), carbon monoxide (CO), methane (CH<sub>4</sub>), and nitrous oxide (N<sub>2</sub>O) is presented. All research campaigns the Quantum Cascade Laser spectrometers (QCLs) have participated in are outlined. The basic operational principle of QCLs is discussed. Finally, the calibration approach and in-flight performance are outlined.

## 4.1 Introduction

A new instrument for airborne measurements of carbon dioxide, carbon monoxide, methane, and nitrous oxide (Quantum Cascade Laser Spectrometer [QCLS]) is presented. QCLS was developed through a collaborative effort between Aerodyne Research Inc. and the Wofsy group. High precisions and accuracies with fast time response are achieved with direct absorption spectroscopy in mid-infrared (IR) region. The package has been designed to integrate easily onto multiple aircraft platforms, and sample from the surface to the middle stratosphere.

**Table 4.1** Aircraft deployments **with the QCLS.**

Campaign	Date	Location	Coverage	Objective
START08	April-June 2008	Broomfield, CO NCAR GV	25-65°N 80-120°W 0-14.3 km	Transport processes in the extratropical upper troposphere and lower stratosphere
HIPPO-1	January 2009	Pole to Pole NCAR GV	-70-85° 0-14.3 km	Global mapping of greenhouse gases stretching pole to pole and ranging from surface to tropopause
HIPPO-2	October-November 2009	Pole to Pole NCAR GV	-70-85° 0-14.3 km	Global mapping of greenhouse gases stretching pole to pole and ranging from surface to tropopause
HIPPO-3	March-April 2010	Pole to Pole NCAR GV	-70-85° 0-14.3 km	Global mapping of greenhouse gases stretching pole to pole and ranging from surface to tropopause
CALNEX	April-June 2010	Ontario, CA NOAA P-3	32-40°N 116-124°W 0-6.5 km	Regional air quality and climate assessment

The first field deployment of QCLs occurred in spring of 2008 as part of the START08/pre-HIPPO (Stratosphere-Troposphere Analyses of Regional Transport/Hiaper Pole to Pole Observations) campaign based out of Broomfield, CO on the HIAPER Gulfstream-V (GV) aircraft (Pan et. al., 2010). Since this first deployment, QCLs has flown successfully from pole to pole on three separate campaigns (HIPPO-1 (Wofsy et. al., 2011), HIPPO-2, HIPPO-3) based on the GV, as well as on the NOAA P-3 aircraft for the CALNEX (California at the Nexus of Air quality and Climate Change) campaign in spring of 2010. See Table 4.1 for complete list of campaigns flown.

## 4.2 Instrument Design

The QCLs package consists of two independent spectrometers, one dedicated to measurement of CO<sub>2</sub> (henceforth referred to as QCO<sub>2</sub>), and the second dedicated to CO, CH<sub>4</sub>, and N<sub>2</sub>O (henceforth referred to as DUAL, referencing the number of lasers in the spectrometer). The optical layout is as developed, designed, and sold by Aerodyne Inc (Herndon et. al., 2007). The remainder of the instrument (temperature control, pressure control, electronics, mounting, attachment of optical pieces) y cu custom designed cvJ ctxctf "for aircraft operation. The total package integrated on the GV can be seen in Figure 4.1. The two spectrometers have independent optical systems and flows, sharing only the downstream pump, chilled fluid for laser cooling, and control computers. Master control is performed by a robust datalogger (CR-10x, Campbell Scientific), in a similar manner to that of the Harvard CO<sub>2</sub> instrument (Daube et. al., 2002). The CR-10x collects all housekeeping data and controls the data acquisition computer. The data acquisition computer controls and records all elements relating to spectroscopy. Both spectrometers are mounted on temperature-stabilized, vibrationally isolated optical benches with heated covers. Sample air, taken in through independent rear-facing inlets, is preconditioned



**Figure 4.1** Full QCLS package integrated on the GV.

with a Nafion drier (to remove the bulk of water vapor), and passed through a dry ice water trap reducing sample air dew-point to less than -70 Celsius prior to detection. This eliminates any potential interference of water vapor absorption features, and allows direct retrieval of dry mole fraction.

Absorption spectra of strong ro-vibrational transitions in the mid-infrared are measured using pulsed quantum cascade (QC) lasers. Thermo-electrically cooled (TEC), distributed feedback (DFB) InGaAs-InAlAs/InP QC lasers (Alpes Lasers) are used. The lasers are operated at very low duty cycles, ~1%, with short pulses, ~12 ns. Lasers are tuned over designated spectral windows by modulating QC laser temperature with a sub-threshold current ramp. Laser sink temperature is held constant to better than 1 mk/Hz<sup>2</sup> with a two-stage Peltier module, maintaining a stable center on the scan window. Laser light is collimated and directed into sampling cells operating at reduced pressure (~50 torr). Light exiting the cell is directed into Liquid Nitrogen (LN<sub>2</sub>) cooled photovoltaic detectors (HgCdTe for DUAL, InSb for QCO<sub>2</sub>). The absorption feature is fit, and HITRAN linestrengths (Rothman et. al., 2005) are used to convert absorbance to number density, which is in turn converted to dry mole fraction with retrieved pressure and temperature values.

#### **4.2.1 QCO<sub>2</sub>**

The CO<sub>2</sub> measurement is based on a differential absorption technique. The laser is scanned over the CO<sub>2</sub> absorption feature at 2319.18 cm<sup>-1</sup> over a 0.3 cm<sup>-1</sup> range (figure 4.2). This line is chosen for its minimal temperature dependence. The strength of CO<sub>2</sub> absorption at this wavenumber requires the QCO<sub>2</sub> spectrometer to be enclosed in a sealed pressure vessel purged with ultra-pure, CO<sub>2</sub>-free nitrogen before operation. The optical layout of QCO<sub>2</sub> is illustrated in Figure 4.3.

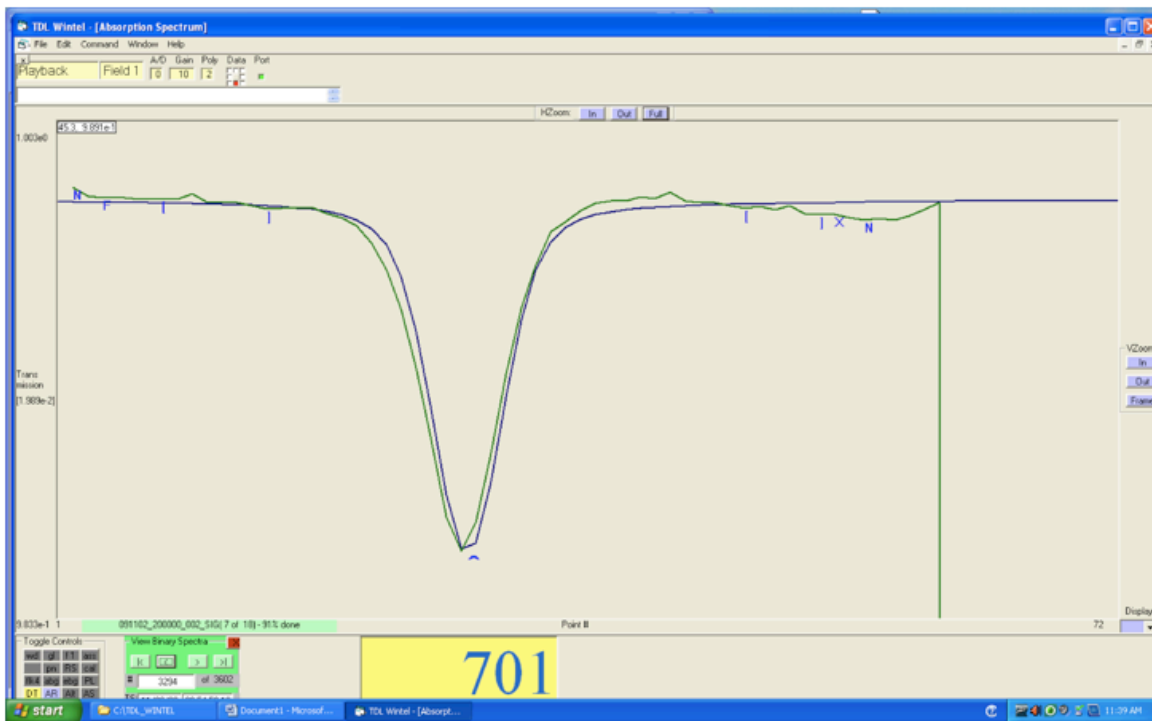


Figure 4.2 Screenshot of TDLWintel showing retrieval of QCO<sub>2</sub> spectrometer measuring a calibration gas, with measurement in green and fit in blue.

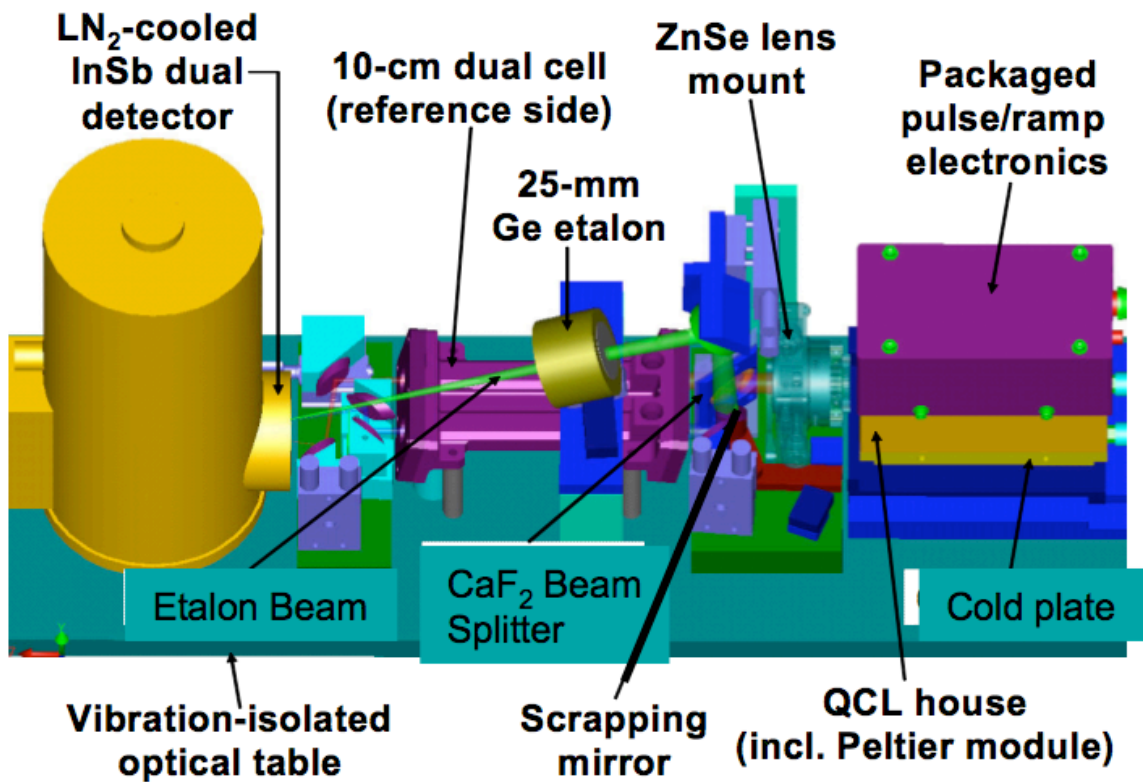


Figure 4.3 Rendering of QCO<sub>2</sub> optical table.

The optical path is straightforward, as the QCL beam is collected and focused by an aspheric ZnSe lens, split by a CaF<sub>2</sub> beam splitter, the two beams traveling through the 10 cm sample and reference cells (both operated at 50 torr and maintained at equal pressure) respectively, and then focused onto the LN<sub>2</sub> cooled InSb detector. There is the option to manually swivel a mirror into the sample path, redirecting this beam through a Ge-etalon for calculation of the laser tuning rate. The measured sample spectrum is divided by the reference spectrum. This approach eliminates common sources of noise (eg laser power fluctuations) as well as reducing proportional noise, as the gas flowed through the reference cell is chosen to be representative of atmospheric CO<sub>2</sub> abundance. The residual absorbance feature is fit with Aerodyne Inc. TDLWintel software, using a non-linear reduced chi-square fit. Information of the line properties (from HITRAN, Rothman et. al., 2005) and laser spectral line-widths (calculated) are used to retrieve dry mole fraction of CO<sub>2</sub>, with an assigned constant temperature and pressure in flight. Real-time data are reported in-flight from this spectral fitting; post-flight data analysis includes refitting all spectra with known pressure and temperature. Frequent in-flight calibrations using known mixing ratios are traceable to WMO standards.

#### 4.2.2 DUAL

The DUAL measurement is also based upon direct absorption spectroscopy. Two TEC, DFB pulsed QCLs are employed in the dual. One is tuned over a CO line at 4.6 μm (2169 cm<sup>-1</sup>, width 0.25 cm<sup>-1</sup>) the other scans over lines of both CH<sub>4</sub> and N<sub>2</sub>O at 7.8 μm (1275 cm<sup>-1</sup>, width 0.35 cm<sup>-1</sup>), figure 4.4. Atmospheric abundances and absorption line strengths of these gases at these wavelengths do not require a purged pressure vessel, but do necessitate the use of a 76 m path length multi-path Herriot cell (McManus et. al., 2007). The cell is 32 cm long, with a volume of 0.5 L, reaching the long path-length via 238 passes. The optical layout for the DUAL can be seen in Figure 4.5. Both laser outputs are collected and focused by reflective Schwarzschild objectives. The beams are

multiplexed both spatially and temporally as to not interfere with each other. A BaF<sub>2</sub> beam splitter is employed to split the beam three ways: primary sample beam (transmitted), pulse-normalization beam (front reflection), and line-lock beam (back reflection). The primary sample beam is passed through the multi-pass cell holding the sample air at 50 torr. The pulse-normalization beam experiences the same external optical path as the sample beam, and is divided by the sample spectra, thus eliminating pulse-to-pulse noise from the measured spectrum. The line-lock beam is passed through a sealed reference cell containing N<sub>2</sub>O and CO, and this measured spectrum is used to locate the spectral location of the absorption lines. All paths in the end lead to LN<sub>2</sub> cooled HgCdTe detectors.

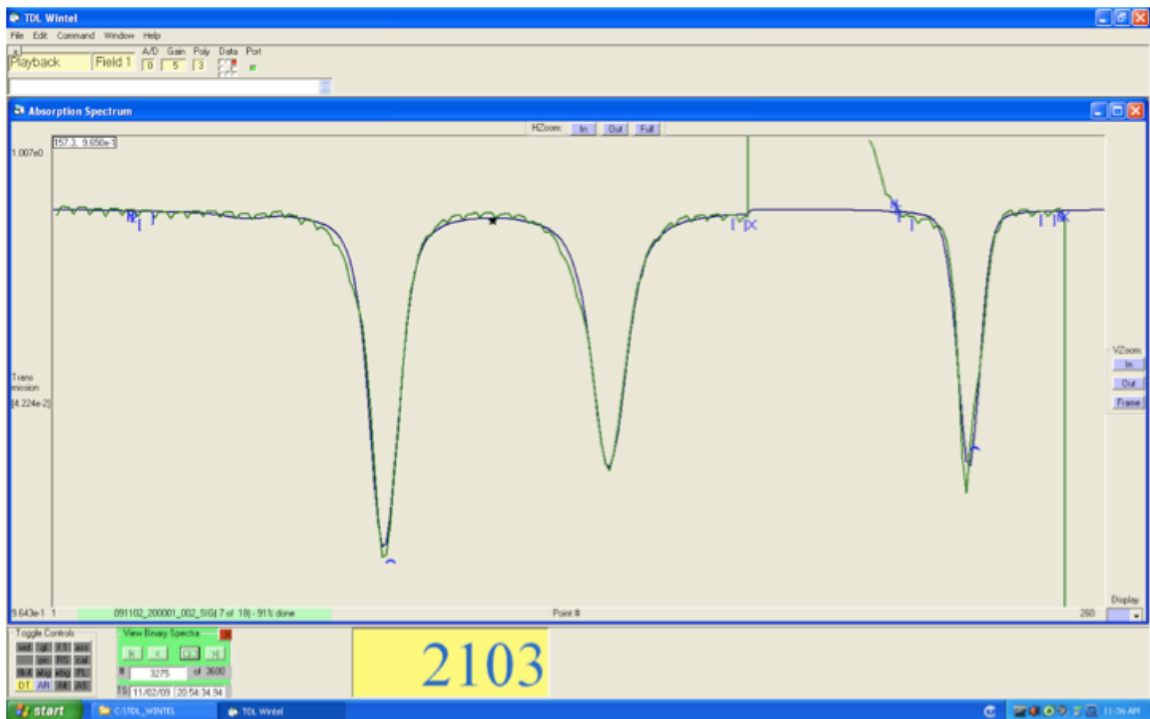


**Figure 4.4** Screenshot of TDLWintel showing retrieval of DUAL spectrometer measuring a calibration gas, with measurement in green and fit in blue, for CH<sub>4</sub>, N<sub>2</sub>O, and CO, from left to right respectively.

As with the CO<sub>2</sub> spectrometer, TDLWintel performs spectral fitting, and frequent in-flight calibrations are performed. Post-flight analysis includes observed pressure and temperature and uses calibrations to adjust mole fractions onto the WMO scale.



reference gas. Since QCO<sub>2</sub> makes a differential measurement, the reference cell always has reference gas flowing, and a 'zero' spectrum is obtained by flowing the same gas through both reference and sample cells. For the DUAL a zero spectrum is obtained by flowing gas with no CO, CH<sub>4</sub>, or N<sub>2</sub>O through the system. In standard operation, a zero is recorded every 15 minutes, and the retrieved zero values are interpolated through the entire flight and subtracted from retrieved values as an offset. Every 30 minutes a high and low span gas is measured in flight. These gases are calibrated before and after every mission directly against standards measured by NOAA. The assigned values for the gases are used to correct the retrieved mole fraction in-flight, placing the measurement onto the WMO scale. Excellent linearity of the QCLS system enables the use of two-point calibrations covering a large dynamic range. An example of in-flight calibration can be seen in figures 4.6 and 4.7.

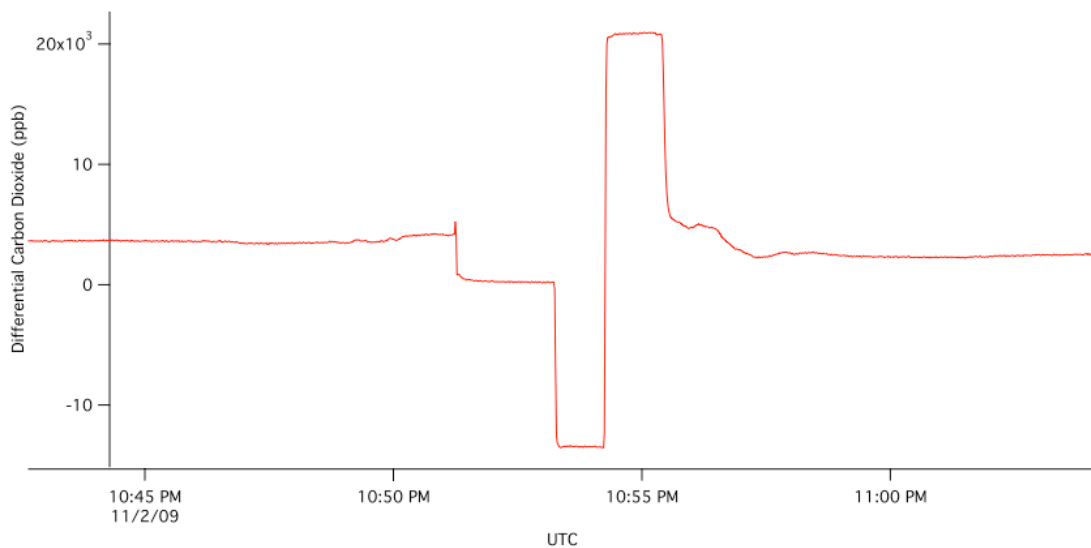


**Figure 4.6** Raw in-flight time series showing full calibration cycle for  $\text{CO}_2$ .

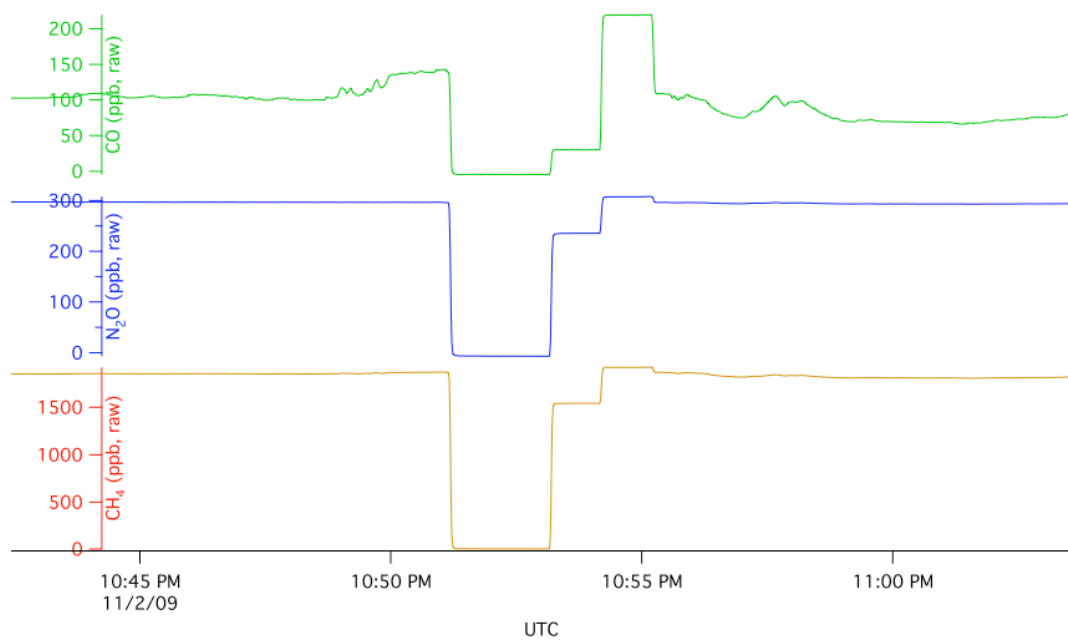


**Figure 4.7** Raw in-flight time series showing full calibration cycle for  $\text{CO}$ ,  $\text{N}_2\text{O}$ , and  $\text{CH}_4$ .

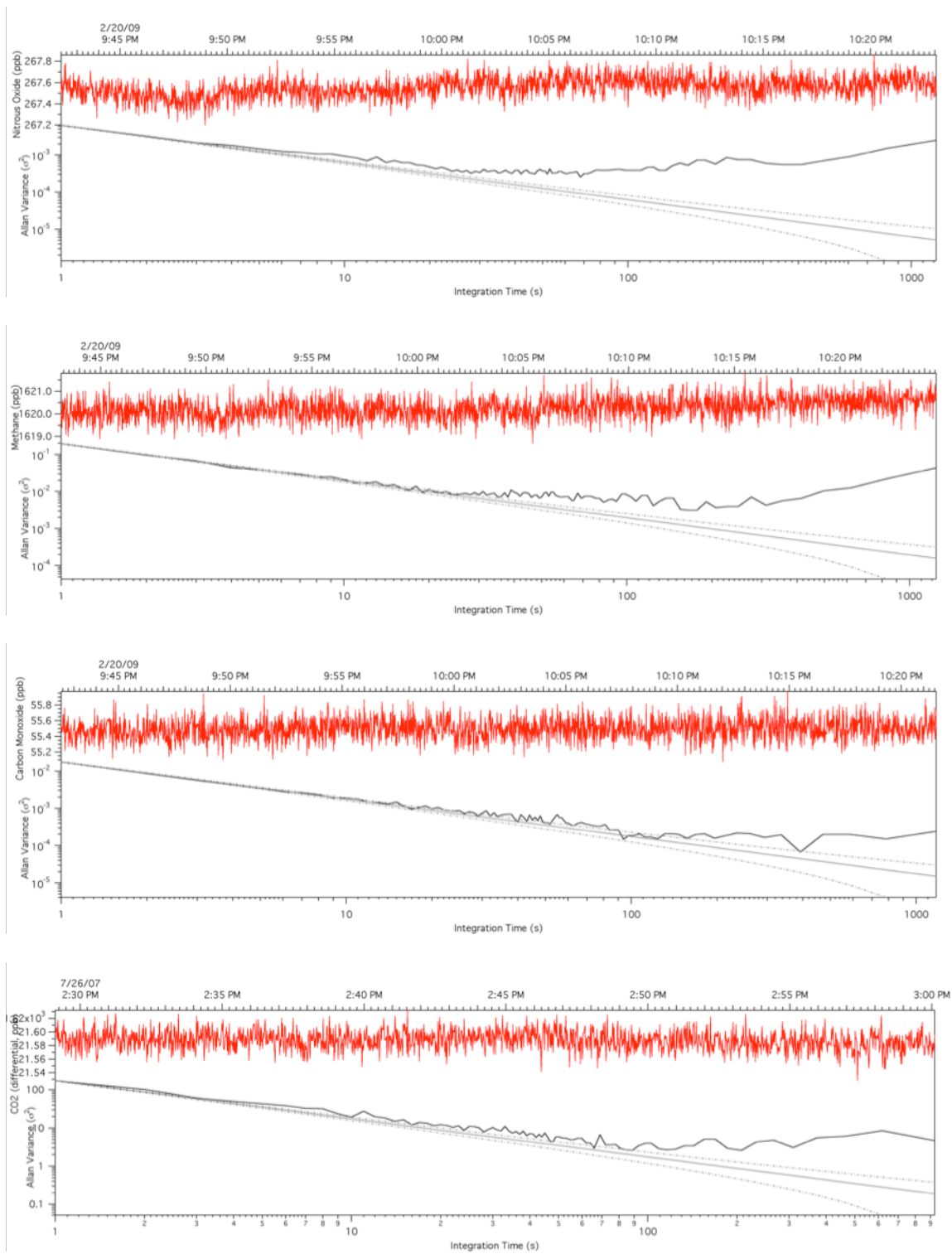


**Figure 4.8** Allan-variance for all four species measuring tank air in lab tests.

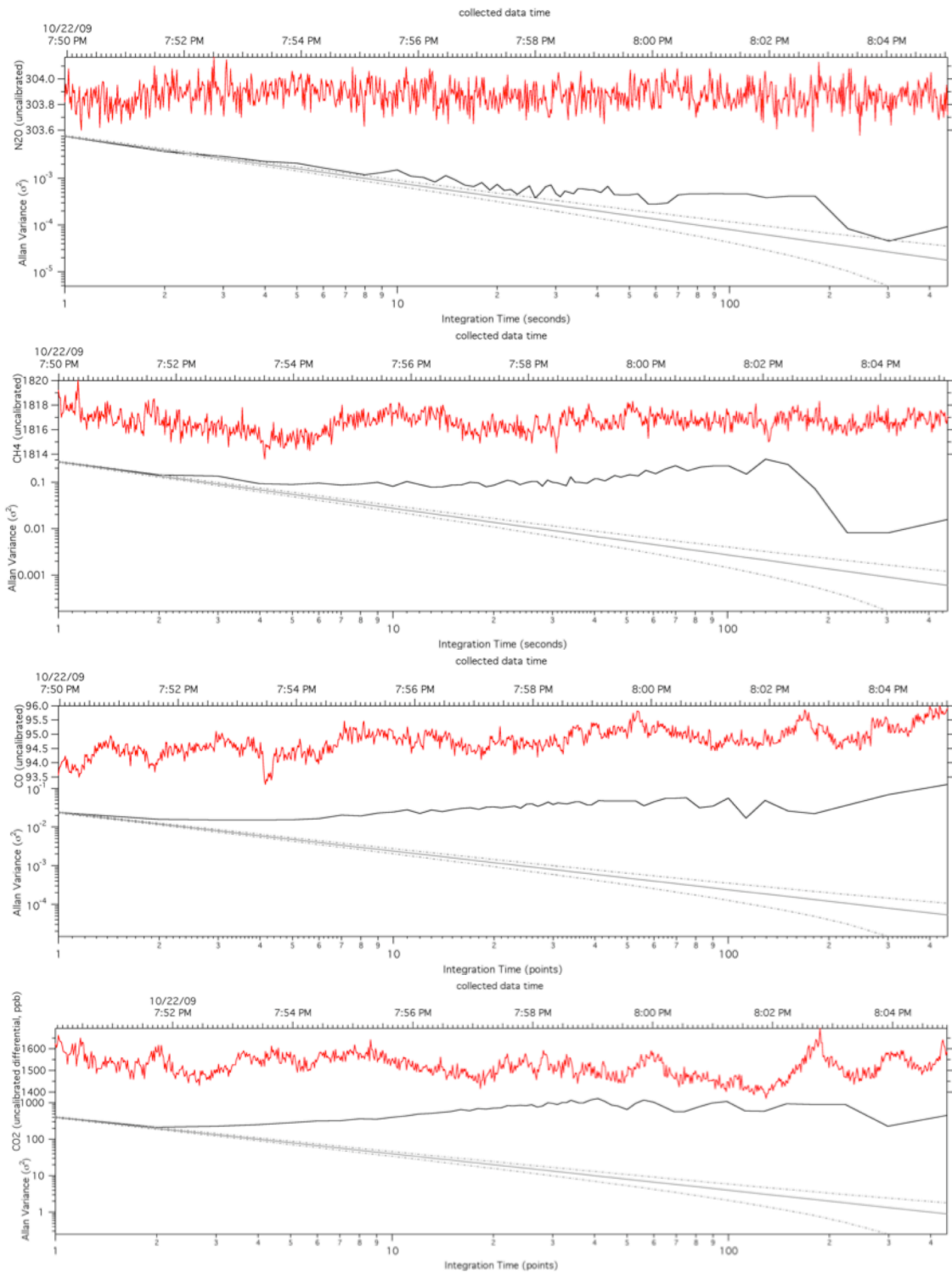


**Figure 4.9** Allan-variance for all four species measuring relatively constant/equilibrium in flight.

## 4.4 Performance

QCLs exhibits unmatched precision for all four tracers. Measuring tank air of constant and known value in the lab provides the basis for assessing instrument performance. Figure 4.8 shows allan-variance plots, and Table 4.1 highlights the corresponding performance metrics. One-second performance exhibits very high

Table 4.1

(ppb)	1 sec	60 sec	Minimum	Abundance
Nitrous Oxide	0.08	0.02	0.02 (63 sec)	270
Methane	0.44	0.09	0.06 (177 sec)	1620
Carbon Monoxide	0.08	0.02	0.0008 (392 sec)	55
Carbon Dioxide	13.21	2.32	1.62 (89 sec)	20,000 (differential)

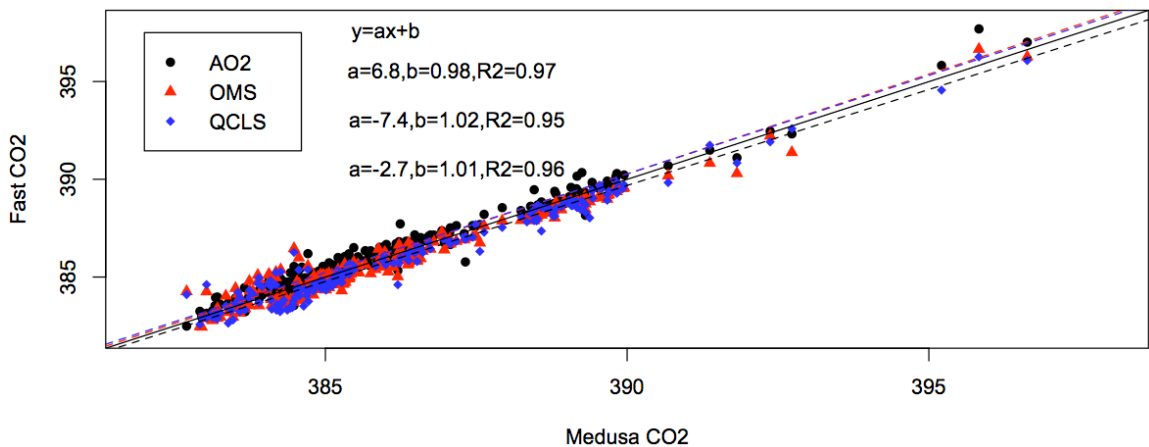
precision, and the instrument exhibits such stability that allan-variance closely follows the behavior of white noise, with time series of greater than 30 minutes exhibiting no drift. Figure 4.9 shows raw traces collected in-flight, with the associated allan-variance plot. We encountered a relatively constant air mass for this time frame, particularly for N<sub>2</sub>O, which in this instance experiences an allan-minimum even better than seen in lab, of 0.007 ppb at 300 seconds. Some true atmospheric structure is seen for the other gases, preventing the allan-variance from improving with time in the same manner as the lab study. This time-series serves as an ideal example of actual instrument performance in-flight. Table 4.2 summarizes the in flight precision, as well as instrument accuracy, determined based on calibration tanks. It is important to note the one-second precision is almost identical in flight measuring external air as in the lab measuring a tank, demonstrating the robustness of the instrument to aircraft environments.

Table 4.2

Species	Precision (1 $\sigma$ , 1sec, ppb)	Accuracy (1 $\sigma$ , ppb)
Nitrous Oxide	0.09	0.2
Methane	0.5	1
Carbon Monoxide	0.15	3.5
Carbon Dioxide	20	100

## 4.5 In-flight instrument comparison

On HIPPO-1, other instruments also made measurements of all four species observed by QCLs. Carbon Dioxide, one the target gases of HIPPO, was measured by three different 1-Hz in-situ analyzers (QCLs, Harvard CO<sub>2</sub> (LiCor based system, reported accuracy and precision 0.1 ppm, PI: Steve Wofsy, Daube et. al., 2002), and AO<sub>2</sub> (LiCor based system, PI: Britt Stephens)). There also were flasks measured by NOAA and Scripps (MEDUSA, PI: Ralph Keeling), though HIPPO-1 NOAA flasks were contaminated with water, and only MEDUSA flasks are considered here. All systems were calibrated and tied to WMO scale, with the pairs QCLs-Harvard CO<sub>2</sub> and AO<sub>2</sub>-MEDUSA sharing secondary standards. The relationship between all fast observations and MEDUSA flasks is found to be linear with slight differences between analyzers (figure 4.10). Box and whisker plots show median flask and fast response analyzers do



**Figure 4.10** Fast CO<sub>2</sub> analyzers compared with flask measurements.

not agree as well as desired (figure 4.11). Offset compared to flask observations are ~0.4 ppm, and opposite directions for the Harvard sensors compared to AO<sub>2</sub>. Comparison between fast sensors only shows excellent agreement between Harvard sensors, with an offset of ~0.4 ppm relative to AO<sub>2</sub>. These scale discrepancies are difficult to explain, but re-calibration of Harvard standards by NOAA indicate Harvard sensors are indeed on WMO scale. Reassuringly, there is tight agreement between OMS and QCLS, indicative

that the flight instrument is operating in a precise and stable manner, and the offset is attributable to **ground** calibration offsets between Scripps and Harvard, not the in-flight instrument.

Nitrous Oxide, in addition to QCLs, is measured in canisters of the Whole Air Sampler (WAS, PI: Eliot Atlas), as well as two onboard gas-chromatographs (PANTHER and UCATS, PI: Jim Elkins). QCLs agrees well with WAS and PANTHER, with an offset of less than 0.26 ppb (within WAS and PANTHER accuracies of ~1%). An offset of 1.3 ppb is found relative to UCATS, within reported UCATS uncertainty (~1%) and likely due to water interference on N<sub>2</sub>O in UCATS (figure 4.12).

Methane can be compared with the same samples (WAS, PANTHER, UCATS). QCLs shows an offset of less than 0.2 ppb relative to UCATs, very close agreement well within uncertainty. Larger offsets are found relative to WAS (16 ppb) and PANTHER (12 ppb), but these still lie within 1% accuracies of these measurements (figure 4.13).

Carbon Monoxide can be compared with WAS and PANTHER, as well as another fast response instrument- a VUV-CO analyzer from NCAR (PI: Teresa Campos). Some offsets are present, relative to WAS (2.3 ppb), RAF (3.5 ppb), and PANTHER (2.3 ppb), all within reported accuracies. **O wej "qh'yj g"4/ugpuqt"xctkpeg'ctkugu'ltqo 'lko g'tgur qpug'f khtgpeg0**

For in-flight comparisons, we find tight agreement within uncertainties for CH<sub>4</sub>, N<sub>2</sub>O, and CO. For CO<sub>2</sub>, we find a scale offset between different analyzers, attributable to ground calibration offsets and not the flight instrument. Taken together these comparisons validate the flight observations from QCLS, demonstrate it is possible to maintain well calibrated observations while flying around the globe with minimal support, and highlight the importance of ground calibrations in bring disparate observations in agreement.

## 4.6 Conclusion

In this chapter, the new instrument QCLs was presented. All research campaigns are mentioned, and the instruments flexibility to be deployed on multiple platforms (GV, P-3) as well as challenging field environments (HIPPO campaigns) is demonstrated. The fundamental operational principle of the instrument is discussed, in addition to details on the optical set-up. The calibration approach, linking observations to global WMO scale, and validation with other instruments is discussed. Finally, in-field performance is highlighted, demonstrating the extreme high-precisions achieved (20 ppb CO<sub>2</sub>, 0.15 ppb CO, 0.5 ppb CH<sub>4</sub>, 0.09 ppb N<sub>2</sub>O) in a challenging environment.

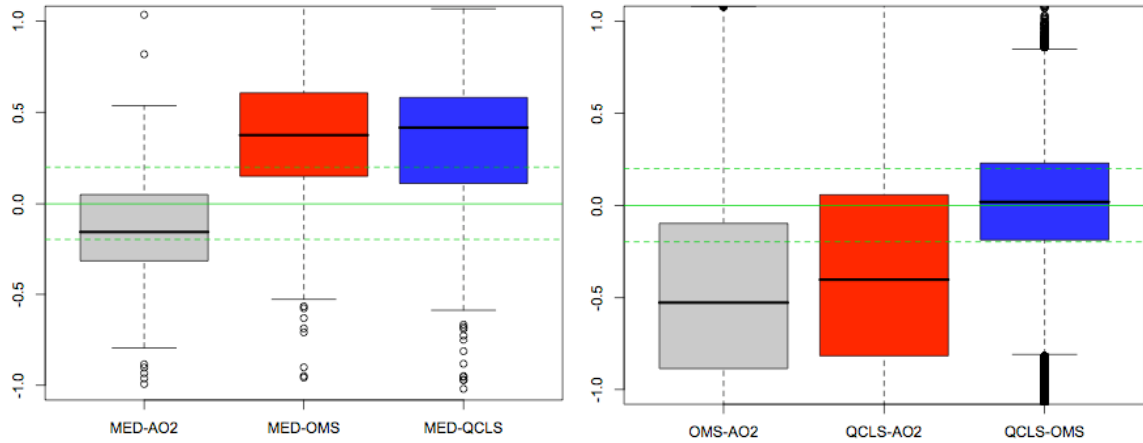


**Figure 4.11** Box and whisker plots of CO<sub>2</sub> residuals (ppm) comparing to MEDUSA (left) and between fast samplers (right). The green line shows zero, and dashed green lines show  $\pm 0.2$  ppm.

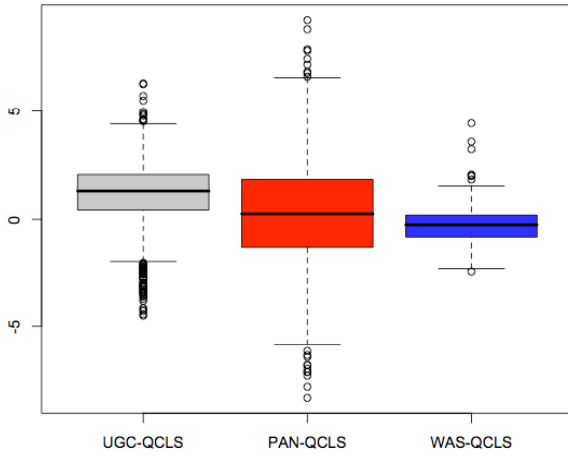


**Figure 4.12** Box and whisker plots of N<sub>2</sub>O residuals

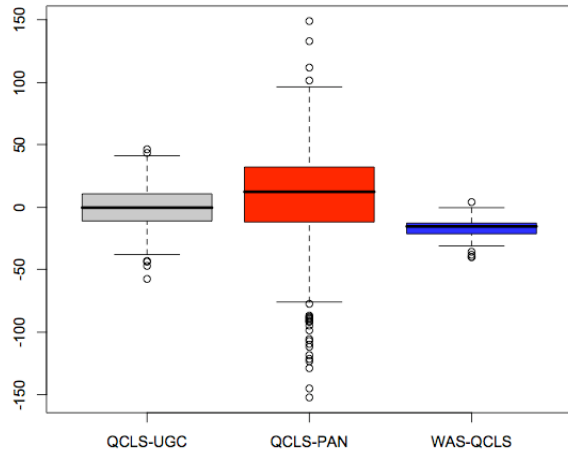


**Figure 4.13** Box and whisker plots of CH<sub>4</sub> residuals

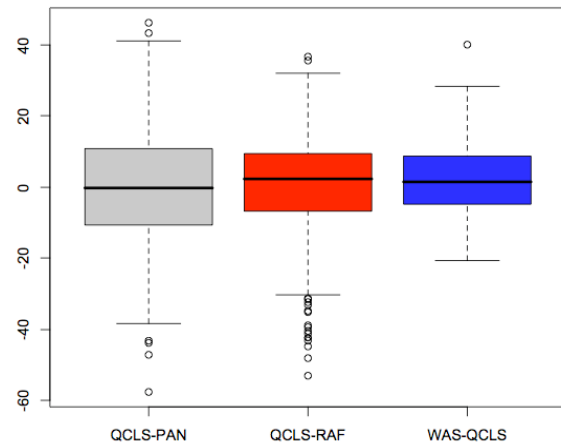


**Figure 4.14** Box and whisker plots of CO residuals

## References Cited

- Daube, B. C., K. A. Boering, A. E. Andrews, and S. C. Wofsy (2002), A high-precision fast-response airborne CO<sub>2</sub> analyzer for in situ sampling from the surface to the middle stratosphere, *Journal of Atmospheric and Oceanic Technology*, 19(10), 1532-1543.
- Herndon, S. C., M. S. Zahniser, D. D. Nelson, J. Shorter, J. B. McManus, R. Jimenez, C. Warneke, and J. A. de Gouw (2007), Airborne measurements of HCHO and HCOOH during the New England Air Quality Study 2004 using a pulsed quantum cascade laser spectrometer, *Journal of Geophysical Research-Atmospheres*, 112(D10), 15.
- McManus, J. B. (2007), Paraxial matrix description of astigmatic and cylindrical mirror resonators with twisted axes for laser spectroscopy, *Applied Optics*, 46(4), 472-482.
- Pan, L. L., et al. (2010), THE STRATOSPHERE-TROPOSPHERE ANALYSES OF REGIONAL TRANSPORT 2008 EXPERIMENT, *Bulletin of the American Meteorological Society*, 91(3), 327-+.
- Rothman, L. S., et al. (2005), The HITRAN 2004 molecular spectroscopic database, *Journal of Quantitative Spectroscopy & Radiative Transfer*, 96(2), 139-204.
- Wofsy, S. C., et al. (2011), HIAPER Pole-to-Pole Observations (HIPPO): Fine grained, global scale measurements for determining rates for transport, surface emissions, and removal of climatically important atmospheric gases and aerosols, *Phil. Trans. of the Royal Society A*, in press.

## CHAPTER 5

### **Tropospheric distribution and variability of N<sub>2</sub>O: evidence for strong tropical emissions**

[Kort, E. A., P. Patra, K. Ishijima, B. C. Daube, J. Elkins, D. Hurst, R. Jimenez, F. Moore, and S. C. Wofsy (2011), Tropospheric distribution and variability of N<sub>2</sub>O: evidence for strong tropical emissions, to be submitted *Geophys. Res. Lett.*]

#### **Abstract**

Measurements of atmospheric N<sub>2</sub>O spanning altitudes from the surface to 14 km, and latitudes from 67°S to 85°N, show high concentrations in the tropics and subtropics, with strong maxima in the middle and upper troposphere. The pattern varies significantly over time scales of a few weeks. **Global simulations**

**do not accurately capture observed distributions with latitude,**

**altitude, or time.**

**Global simulations do not accurately capture observed distributions with latitude,**

**altitude, or time. Inversion results indicate significant**

**changes in tropospheric N<sub>2</sub>O (as large as 1 Tg N-N<sub>2</sub>O over 9 weeks).**

**These findings highlight the importance of**

**the tropical troposphere in deriving emissions from atmospheric measurements.**

## 5.1 Introduction

In the last 40 years, increasing concern has developed over humanity's role in affecting atmospheric constituents and resulting consequences. Two areas in particular have garnered much attention from scientists and policy makers alike: stratospheric ozone depletion and global warming. Quantification of climatically relevant trace gas emissions is crucial in both understanding the severity of the problem, and for defining emissions. Using only reported statistics and/or biogeochemical models (so called 'bottom-up' methods) to gauge emissions have severe limitations, and the need for direct atmospheric observations ('top-down' methods) to quantify emissions has been made explicit (Nisbet & Weiss, 2010).

Top-down approaches have taken many different forms. Regional studies, typically of limited spatial and/or temporal scale, have employed total column (Wunch et al., 2009), surface (Thompson et al., 2010), satellite (Bergamaschi et al., 2007), and aircraft observations (Kort et al., 2008; D'Amelio et al., 2009). Global studies of surface and/or satellite observations when inverting for surface fluxes, with aircraft data typically only used for post-inversion comparisons (Stephens et al., 2007; Chevallier et al., 2010) due to spatial and temporal coverage limitations, with a recent exception where upper tropospheric data are used in an inversion (Patra et al., 2011). These post-inversion analyses (Stephens et al., 2007; Patra et al., 2011) have demonstrated that in-situ vertical profiles can contain crucial additional information regarding fluxes.

Here we present in-situ, global scale, surface to stratosphere observations of Nitrous Oxide (N<sub>2</sub>O) collected on the first two HIAPER Pole to Pole Observations campaigns (HIPPO) conducted in January 2009 and November 2009. Nitrous Oxide, presently the single most important anthropogenically emitted stratospheric ozone depleting substance (ODS) (Ravishankara et al., 2009), is the third most potent long-lived anthropogenic greenhouse gas (<http://www.esrl.noaa.gov/gmd/aggi/>). In spite of the important role N<sub>2</sub>O plays in our atmosphere (Forster et al., 2007), and the continuously

increasing atmospheric burden (0.5-0.8 ppb/year on current troposphere abundances of 320-325 ppb; [www.esrl.noaa.gov/gmd/hats/combined/N2O.html](http://www.esrl.noaa.gov/gmd/hats/combined/N2O.html)), our understanding of sources (natural and anthropogenic), their distribution, strength, and seasonality remain poorly quantified due to the lack of in-situ data with adequate resolution and spatial-temporal coverage.

Current global (Prinn et al., 1990; Hirsch et al., 2006; Huang et al., 2008) and regional (Nevison et al., 2004; Kort et al., 2008; 2010) top-down studies of emissions have been performed. Global studies point to northern tropical emissions and decreased southern ocean fluxes (Huang et al., 2008), but surface observations lack spatial and temporal coverage, particularly in tropical and southern regions. The reliance on surface observations perhaps explains why regional studies lack northern mid-latitudes prior inventories too low." with a significant seasonal component (Kort et al., 2008; 2010).

With the HIPPO observations we repeatedly observed enhanced N<sub>2</sub>O at a range of altitudes (5-14 km) over the remote Pacific Ocean. Results indicate strong bursts of tropical emissions are a significant contributor to global nitrous oxide fluxes, and highlight the importance of obtaining full, in-situ tropospheric profiles.

## 5.2 Model & Measurements

Yong et al. atmospheric N<sub>2</sub>O simulations performed at the Center for Climate System Research/National Institute for Environmental Studies/Frontier Research Center for Global Change (CCSR/NIES/FRCGC) atmospheric general circulation based chemistry-transport model (ACTM), as outlined by Ishijima et al., [2010]. The horizontal model resolution is T42 spectral truncation (~2.8° x 2.8°) with 67 sigma-pressure vertical layers from the earth's surface to 90 km. At 6-hourly time intervals, model transport is nudged towards horizontal winds and temperature from JRA-25 at 6-hourly time intervals (Onogi et al., 2007).

Stratospheric losses from photolysis and oxidation reactions are explicitly modeled. Prior emissions are composed of EDGAR4.1 (Emission Database for Global Atmospheric Research (EDGAR), release version 4.1. <http://edgar.jrc/ec/europa.eu>, 2010) for anthropogenic emissions ( $4.3 \text{ TgN yr}^{-1}$ ). Monthly mean ocean fluxes are from Jin and Gruber [2003] ( $3.5 \text{ TgN yr}^{-1}$ ), and annual natural soil fluxes are from EDGAR 2, scaled by a factor of 1.6 to  $10.5 \text{ TgN yr}^{-1}$ . This scaling of the soil fluxes works well to capture a realistic trend of modeled tropospheric  $\text{N}_2\text{O}$  by balancing the total emissions ( $18.3 \text{ TgN yr}^{-1}$ ) and the stratospheric sink [Ishijima et al., 2010]. Sulfur Hexafluoride ( $\text{SF}_6$ ) **ycu** modeled also with ACTM using EDGAR4.1 emission distribution for 2005, with global totals following Levin et al. [2010] through 2008, extrapolated through 2009.

$\text{N}_2\text{O}$  measurements were made *in-situ* by the Harvard/Aerodyne Quantum Cascade Laser Spectrometer (QCLS), one of the Hiaper Airborne Instrumentation Solicitation (HIAS) suite of instruments aboard the GV, retrieved at 1-Hz with  $1\sigma$  precision of 0.09 ppb and accuracy of 0.2 ppb (0.03% and 0.06% at 320 ppb, see supplement for further details).  $\text{SF}_6$  measurements were made *in-situ* every 70 s by the Unmanned aircraft systems Chromatograph for Atmospheric Trace Species (UCATS) 2-channel gas chromatograph with accuracy and precision of 1%.

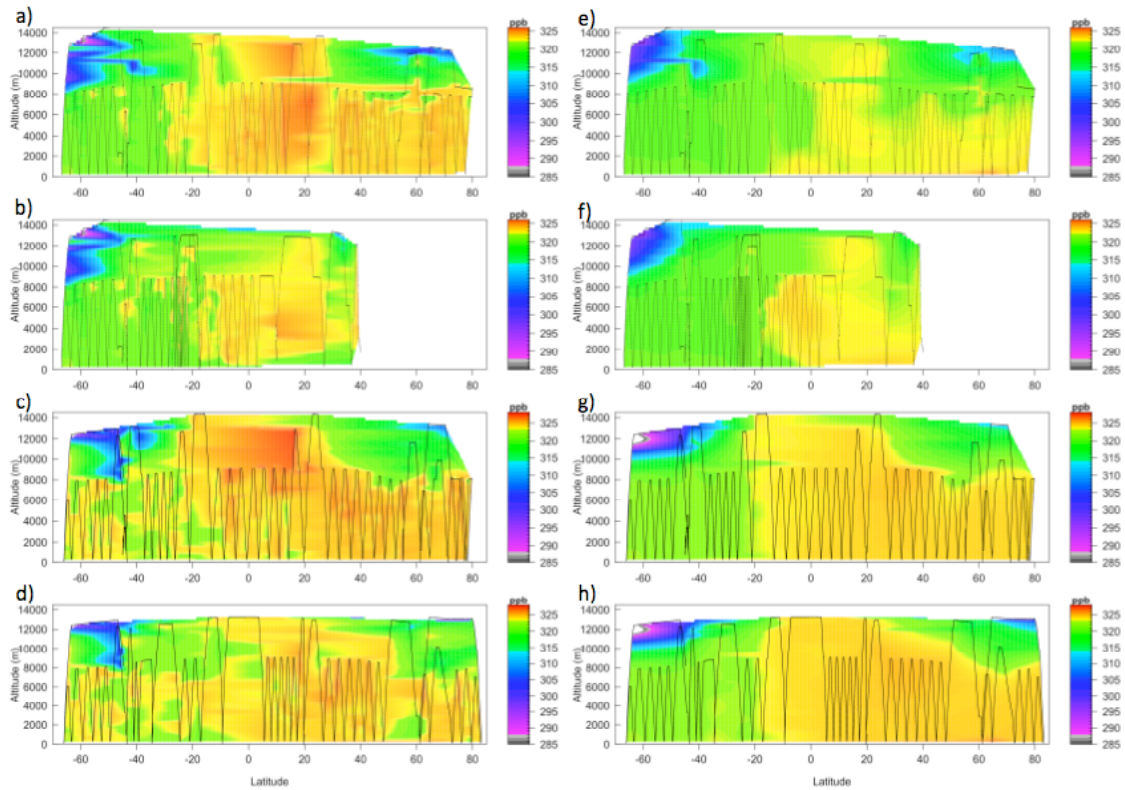


**Figure 5.1** Latitudinal and vertical distributions of  $N_2O$  along HIPPO-1 (January 2009) and 2 (November 2009) transects. a) HIPPO-1 Southbound (SB) observations. b) HIPPO-1 Northbound (NB) observations. c) HIPPO-2 SB observations. d) HIPPO-2 NB observations. e) HIPPO-1 SB model. f) HIPPO-1 NB model. g) HIPPO-2 SB model. h) HIPPO-2 NB model. Flight tracks in black lines.

### 5.3 Results & Discussion

Due to its long lifetime (~120 years, Forster et al., 2007), the distribution of  $N_2O$  is relatively small variability in the troposphere (3-5 ppb superimposed on a background of ~322 ppb in 2009; Fig. 5.1, panels a-d). Global model results produce somewhat similar features (Fig. 5.1, panels e-h), but measurements show notable enhancements at altitude in the tropics and subtropics, first seen along four cross-sections, two along HIPPO-1 transects (cf. Wofsy et al., 2011) and two not present in the simulations. These enhancements were observed in four cross-sections, two obtained in January 2009, and two in November 2009. The variability in  $N_2O$  is even on southbound and northbound legs only separated by days or weeks. Evidently, the

global-scale sources of N<sub>2</sub>O have strong temporal variability not represented in current models.

Model-data comparison enables quantification of information gained with the full tropospheric measurements compared to surface observations. For the purpose of comparing with model output, we bin our observations in 10 degree latitudinal and 500 m vertical bins. Model output is sampled along the flight tracks, and aggregated in the same manner. For HIPPO-1, simulation results agree well with surface observations, so no bias is adjusted in the inverse analysis. For HIPPO-2, the model shows a negative bias relative to surface observations, so a tropospheric bias of 1.2 ppb is removed.

First we consider only data collected from 250-750 m, **remote surface observations typically used in inversion studies. Latitudinal gradients in the prior model closely match the observed surface layer in both HIPPO-1 (Fig. 5.7a) and HIPPO-2.** We perform a Bayesian inversion using just the 0-1 km data, solving for 12 global regions (similar to Huang et al., 2008) for three different three week time frames, starting six weeks before mission start (pulse 1), three weeks before mission start (pulse 2), and simultaneous with mission start (pulse 3) (for further description of inversion framework see supplemental materials). With the excellent prior agreement, resultant regional emissions changes are found to be small, with little to no statistical significance, and produce optimized model output little changed from the prior (Fig. 5.7b).

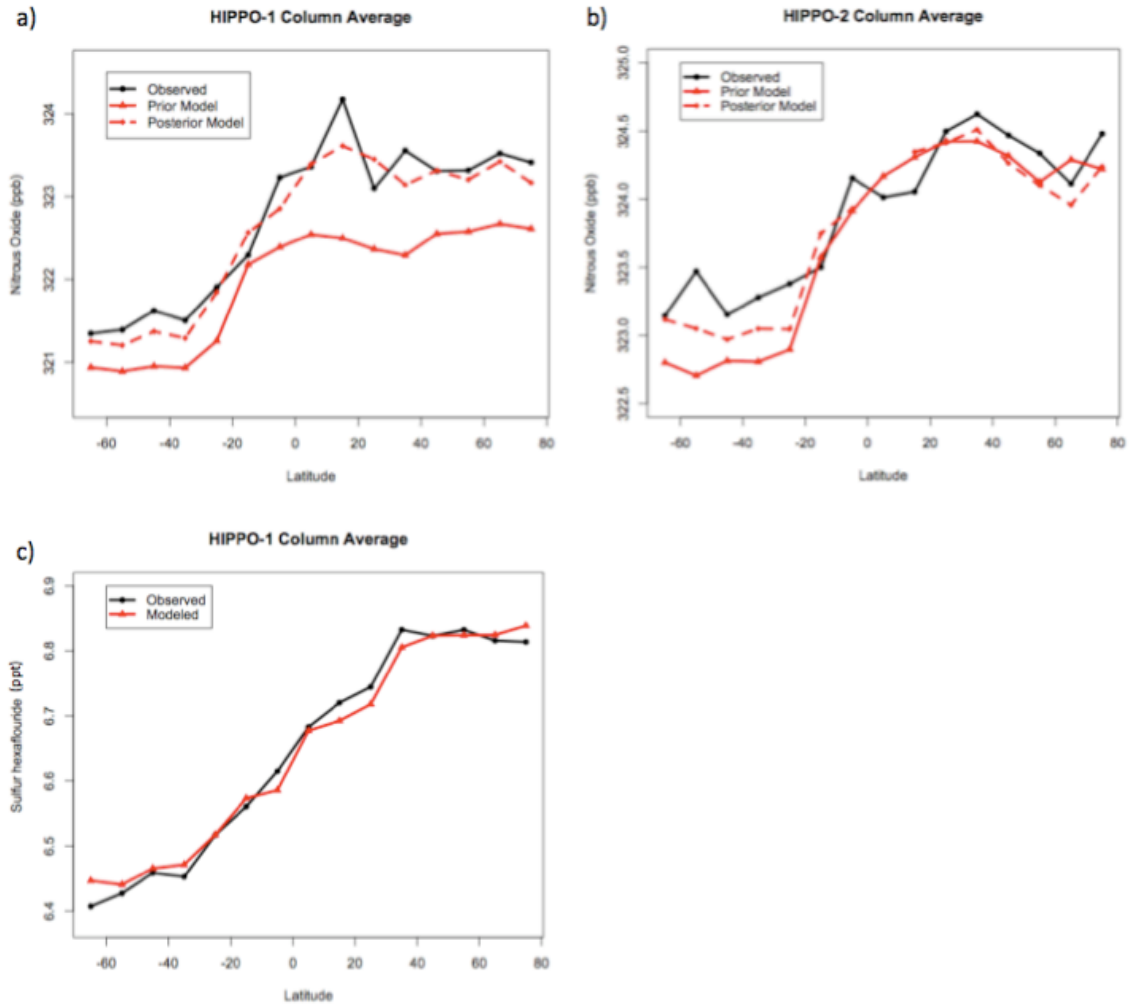


**Figure 5.2** Latitudinal gradients of pressure-weighted column averages. Observations (solid black line), prior model (solid red line line), and optimized model (dashed red line) for HIPPO-1 (a) and 2 (b). Observations (black) and prior (red) model for HIPPO-1 SF<sub>6</sub> (c).

Applying the identical approach instead using the full tropospheric profile results in different conclusions. In spite of excellent agreement found at the surface, modeled HIPPO-1 total column does not match observations in three ways (Fig. 5.2a): 1) Simulations have a low bias. 2) The latitudinal gradient is too small in the model. 3) Enhanced values in northern tropics/sub-tropics are missing. Inversion results produce large changes from prior emissions fields and better reproduce the

observed total column (Fig. 5.2a). A fairly even increase to global emissions addresses the bias. **Strongly increases** to tropical emissions and northern emissions (Fig. 5.3a) corrects for the latitudinal gradient, as well as reproducing the observed ‘bulge’ seen 0-20° N. **Key correction for** the column bias prior to inverting. the net flux increase by 10% due to model increases to northern tropical and higher latitude emissions (addressing the latitudinal gradient and ‘bulge’) remain. Land masses attributed enhanced emissions by the inversion are South America, Africa, and the China/Japan/Southeast Asia regions.

Again, in spite of excellent surface model-data agreement, HIPPO-2 simulated total column results deviate from observations in two ways (Fig. 5.2b): 1) The modeled latitudinal gradient is too strong. 2) Southern hemisphere modeled values are too low. Optimized model results better reproduce observations (Fig. 5.2b) by increasing tropical and southern hemisphere emissions (Fig. 5.3b). Land masses attributed enhanced

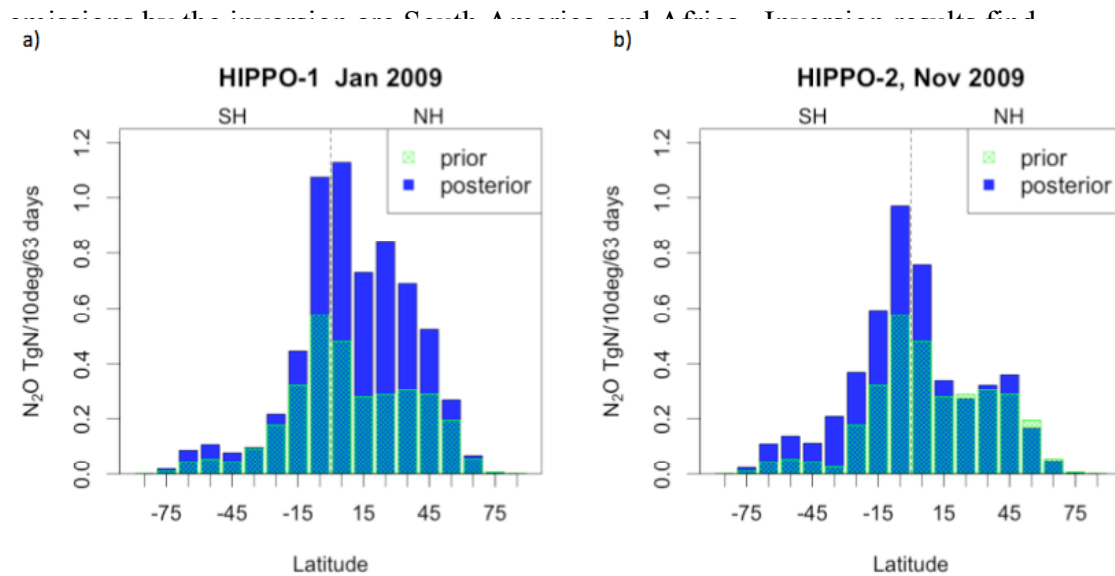


**Figure 5.3** Latitudinal distribution of prior and posterior emissions for HIPPO-1 (a) and HIPPO-2 (b).

significantly enhanced tropical emissions in both January and November, with very different emissions patterns at higher latitudes.

The large **size of these** adjustments, and the strong temporal variability evident in the observed cross sections are consistent with findings of other **recent** top down studies (Kort et al., 2008). It is clear that the enhanced N<sub>2</sub>O seen at altitude is a product of tropical emissions lofted to the middle to upper troposphere by convection. With these observations alone we cannot distinguish whether the actual regional emissions are exhibiting strong temporal dynamics, winking on and off, or **whether strong sources are episodically injected** into the free troposphere by convective activity. **These two sources of variability could be coupled**, as intense rainfall may dramatically stimulate N<sub>2</sub>O production and release from soils, and coincident convection **would** loft these enhanced in N<sub>2</sub>O air parcels to high altitude. This **idea would be consistent with data from** Amazon soils, where N<sub>2</sub>O emissions **were found to vary from negligible to 20 ng-N/(cm<sup>2</sup>hr<sup>1</sup>)**, strongly stimulated by increases in soil moisture (Keller et al., 2005).

**We validated the transport in the model** with SF<sub>6</sub>, a species with a relatively well-known emissions field. Comparisons of modeled column SF<sub>6</sub> with observations show excellent agreement (Fig. 5.2c). This agreement suggests model transport is robust for considering the total column.

. **Considering the vertical gradient in more detail** (Supplemental Fig. 5.4c), the tropical vertical gradient discrepancy present for SF<sub>6</sub> may be a product of over-mixing in model parameterization of convection, which **might help** explain the model's difficulty in representing the extent of the observed reversed vertical gradient of N<sub>2</sub>O (Supplemental Fig. 5.4a,b). If we assumed that the entire discrepancy in the tropical SF<sub>6</sub> vertical gradient **was** caused by transport **errors** (0.1 ppt between 500 & 4500m), and map this 'error' into N<sub>2</sub>O space by comparing **latitudinal gradients** (~0.4 ppt SF<sub>6</sub>, ~2 ppb N<sub>2</sub>O), **this apparent over-mixing** could be responsible for the model underestimating N<sub>2</sub>O at altitude **by 0.5 ppb**, in line with the **optimized** model discrepancy, but **it could not explain the** multiple ppb offset in the prior model. **Thus transport error does not appear to be the major driver of deviance in the prior model.**

## 5.4 Conclusion

Our analysis demonstrates that remote surface observations alone cannot be used for inverse modeling of global  $\text{N}_2\text{O}$  emissions, that global sources are concentrated in the tropics, at least in November and January, and that emissions are highly variable on weekly time scales. It appears that large-scale convective activity lofts enhanced in  $\text{N}_2\text{O}$  air parcels to altitudes ranging 2 to 14 km, from sources over tropical land. Rainfall concurrent with convection may increase tropical soil  $\text{N}_2\text{O}$  production (Keller et al., 2005), amplifying variability in the mid-troposphere. Inverse studies using the ACTM suggest that South America and Africa are large, variable emission sources in both Northern Hemisphere fall and winter (0-5x prior emissions). The region encompassing China, Japan, and Southeast Asia appeared to have very large emissions in January (3-5x prior emissions), possibly a signal of strong agricultural emissions. Future, continuous, high-precision observations in the tropical source regions would be invaluable in distinguishing between variability in emissions and transport, and enable more accurate estimations of annual  $\text{N}_2\text{O}$  emissions.

## 5.5 Acknowledgements

EAK acknowledges financial support from the Department of Defense through the NDSEG fellowship program. HIPPO was supported by NSF grants ATM-0628575, ATM-0628519, ATM-0628388, and by the National Center for Atmospheric Research. The National Center for Atmospheric Research is supported by the National Science Foundation. We would like to thank the pilots, mechanics, technicians, and scientific crew working with the HIAPER aircraft on HIPPO, without whom this research would not have been possible. We thank Xin Jin for providing oceanic flux model results. This work is partly supported by JSPS/MEXT KAKENHI-A grant number 22241008.

## 5.6 Supplemental Materials

### 5.6.1 HIPPO campaign, deployments 1 & 2

The first two HIPPO campaigns consisted of 21 independent flight legs, averaging ~ 8 hrs in duration. Measurements spanned latitudes from 85°N to 67°S, and altitudes from the surface to 14 km. All flights were undertaken by the National Center for Atmospheric Research (NCAR) Gulfstream V (GV) aircraft. The plane is extensively outfitted with a combination of in-situ analyzers and flask samplers, detailed in Wofsy et al., [2011]. Flight tracks for both deployments are illustrated in Figure 5.4. Southbound flights on both campaigns follow very similar routes through the central pacific, while return routing took an eastern excursion on HIPPO-1 with a return to Colorado via Central America, while HIPPO-2 made a western excursion so sample the western pacific warm pool, followed by a return through the north pole flight back to Colorado.

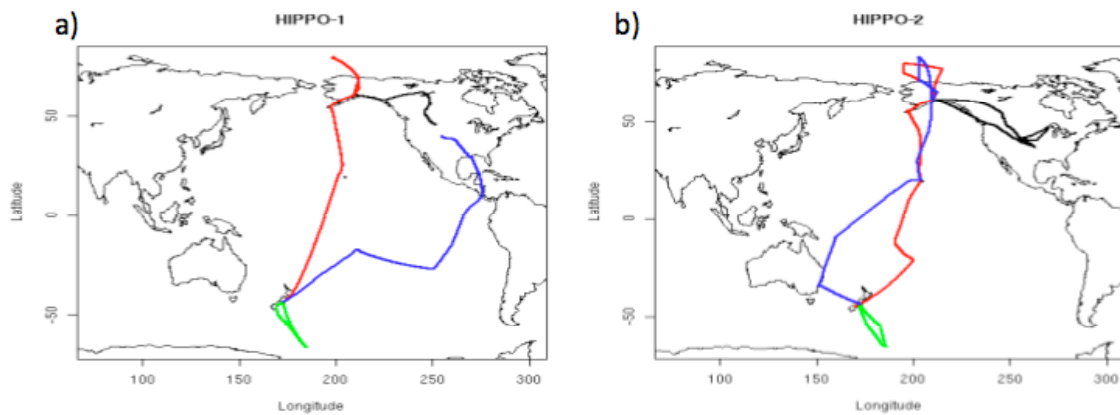


**Figure 5.4** Flight tracks for HIPPO-1 (a) and 2 (b) campaigns. Red shows southbound flights, blue northbound, and green the south pole flight used in the construct of both southbound and northbound cross-sections shown in Figure 1. Black shows continental flights not included in Figure 1.

### 5.6.2 QCLS

QCLS consists of two independent quantum-cascade laser absorption spectrometers, one dedicated to measurement of CO<sub>2</sub>, and the second to CO, CH<sub>4</sub>, and N<sub>2</sub>O, both employing direct absorption spectroscopy (Jimenez et al., 2005; 2006; Herndon et al., 2007). The

in-flight system is frequently calibrated (every 15 minutes one-point calibration, every 30 minutes three-point calibration in standard operation), using calibration gases traceable to World Meteorological Organization (WMO) standards. In-flight performance demonstrated unprecedented in-flight precision and accuracy (Table 5.1). Of particular relevance to this work is the fidelity of the N<sub>2</sub>O measurement, with in-flight performance shown in more detail in Figure 5.2. This stability measuring ambient air with potential real variability serves as an upper limit for in-flight performance. All measurements are given as mole fraction in dry air (‘ppb’ is used as an abbreviation for nmol/mol).

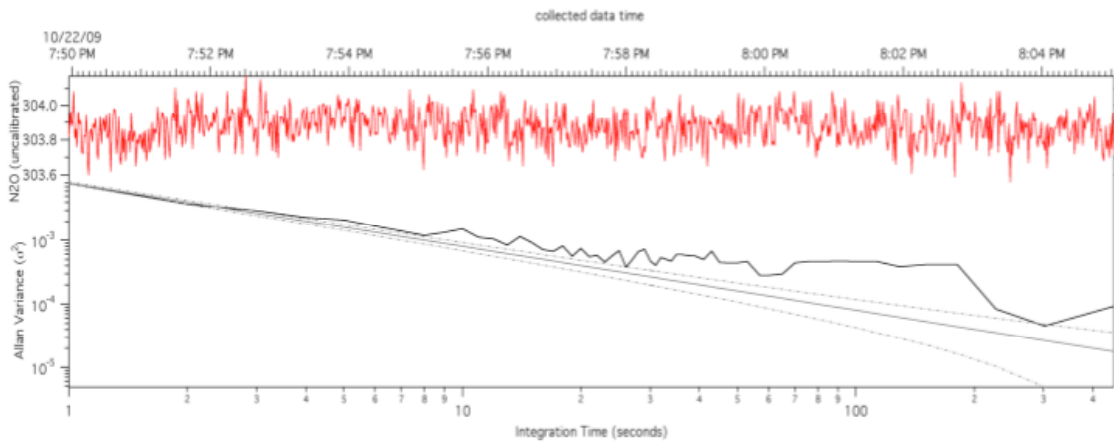


**Figure 5.5:** In-flight measurement of N<sub>2</sub>O encountering relatively constant air mass. Allan-variance showing 1-sec 1 $\sigma$  of 0.09 ppb, and a minimum at 300-sec of 0.007 ppb.

Species	Precision (1 $\sigma$ , 1sec, ppb)	Accuracy (1 $\sigma$ , ppb)
Nitrous Oxide	0.09	0.2
Methane	0.5	1
Carbon Monoxide	0.15	3.5
Carbon Dioxide	20	100

**Table 5.1:** QCLS performance.

### 5.6.3 Inversion Technique

We divide the globe into 12 spatial regions similar to Huang et. al., [2008] for performing inversions (Europe, China/Japan/Southeast Asia, South Asia, Australia/New Zealand, North America, South America, Northwest Asia, Africa, Oceans 30-90°S, Oceans 0-30°S, Oceans 0-30°N, Oceans 30-90°N). To solve the inverse problem, we employ a Bayesian approach, and minimize the following cost function:

$$J(s) = \frac{1}{2}(z - Hs)^T R^{-1}(z - Hs) + \frac{1}{2}(s - s_p)^T Q^{-1}(s - s_p) \quad (S1)$$

Here  $z$  is a  $m \times 1$  vector representing the observed signal.  $s_p$  is the prior scaling factors by region ( $n \times 1$  vector).  $R$  is the model-data mismatch matrix ( $m \times m$ ), and  $Q$  the prior scaling uncertainty ( $n \times n$ ).  $H$  is the Jacobian, representing the sensitivity of observed signal to each source region. To generate  $H$ , 3-week pulses of 1Tg N (as N<sub>2</sub>O) are tagged and tracked for each of the 12 spatial regions for the 3 pulse time frames (6-3 weeks prior, 3 weeks prior to missions start, mission start to 3 weeks).

For the inversion, first we select for only non-continental (research flights 3-10 on HIPPO-1, research flights 2-10 on HIPPO-2) troposphere data in the measurements and model by removing any observations or modeled values less than 320 ppb. (Sensitivity studies show increasing the cutoff value does not change pattern of results). Data is then aggregated into 10-degree latitude and 500 meter vertical bins.  $z$  is formed by removing the prior model results from observations. Prior scaling ( $s_p$ ) is set to zero. Model-data mismatch ( $R$ ) is defined as a diagonal matrix with variance of the sum of a constant error (measurement accuracy) at 0.04 ppb<sup>2</sup> and the variance in observations within the aggregated bin. The prior scaling uncertainty ( $Q$ ) is defined as a diagonal matrix with the variance defined as 3-week's emissions for each region, equivalent to 100% prior error. We then solve the following equations for the optimized scaling factors ( $\hat{s}$ ), and corresponding uncertainties ( $v_s$ ).

$$\hat{s} = s_p + (H^T R^{-1} H + Q^{-1})^{-1} H^T R^{-1} (z - H s_p) \quad (S2)$$

$$v_s = (H^T R^{-1} H + Q^{-1})^{-1} \quad (S3)$$

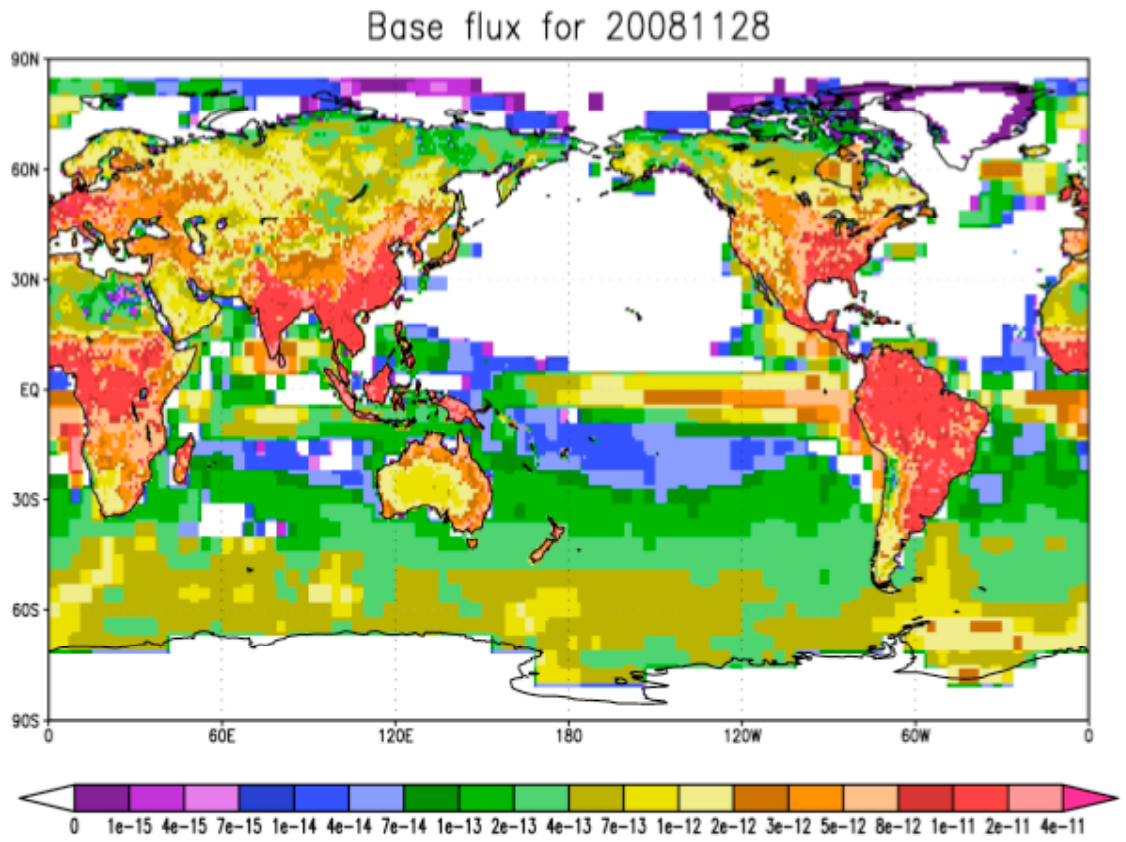


**Figure 5.6:** Distribution of prior source field just prior to HIPPO-1.

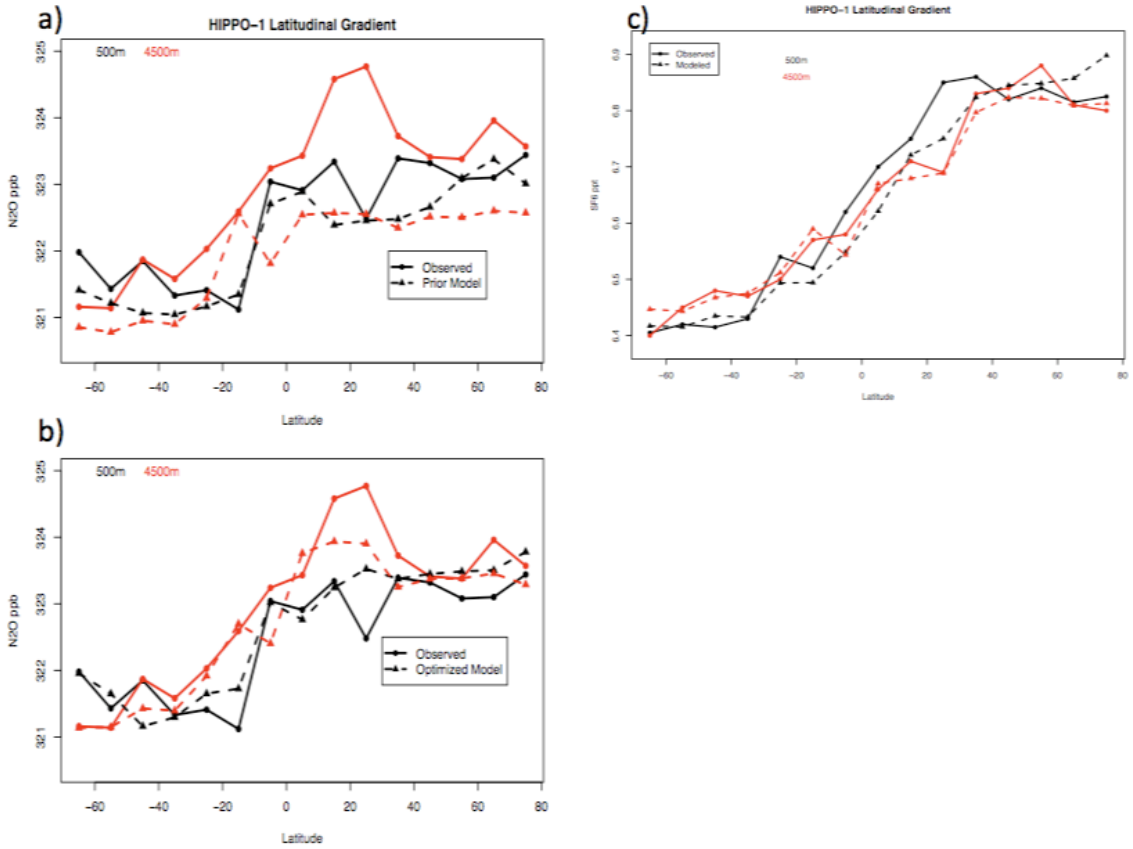


**Figure 5.7:** a) Latitudinal distributions of  $N_2O$  for HIPPO-1 at two 500m-thick altitude layers centered at 500m (black) and 4500m (red), for observations (solid), and prior model (dashed). b) Same as (a) except with optimized model (dashed). c) Same as (a), except for  $SF_6$ .

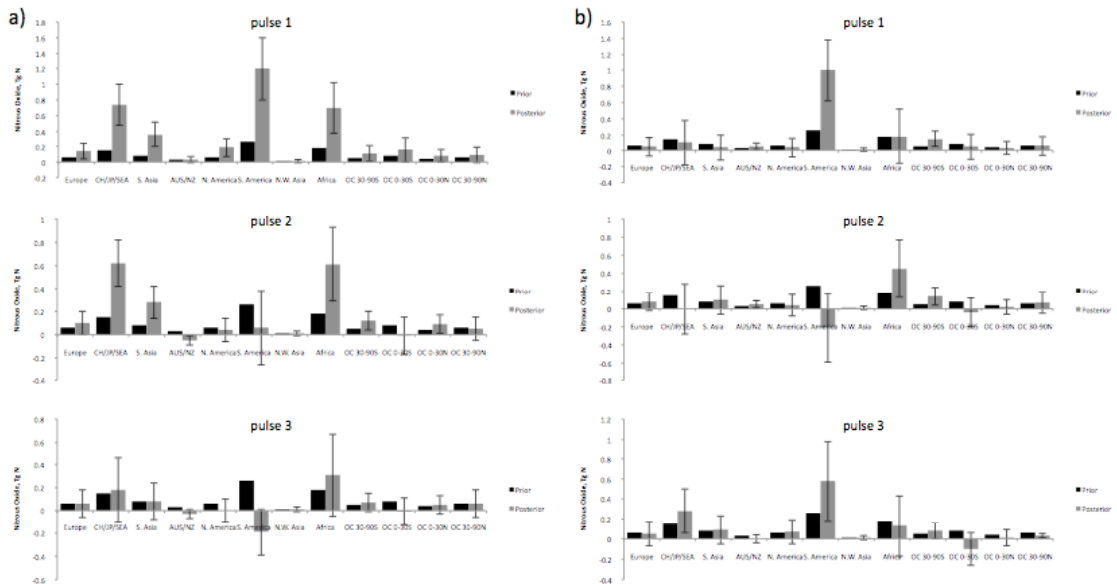


**Figure 5.8:** Entire prior and posterior emissions for three pulses, 12 global regions, with  $2\sigma$  posterior uncertainty for HIPPO-1 (a) and HIPPO-2 (b).

### References Cited

- Bergamaschi, P., et al. (2007), Satellite cartography of atmospheric methane from SCIAMACHY on board ENVISAT: 2. Evaluation based on inverse model simulations, *Journal of Geophysical Research-Atmospheres*, 112(D2).
- Chevallier, F., et al. (2010), CO<sub>2</sub> surface fluxes at grid point scale estimated from a global 21 year reanalysis of atmospheric measurements, *Journal of Geophysical Research-Atmospheres*, 115, 17.
- D'Amelio, M. T. S., L. V. Gatti, J. B. Miller, and P. Tans (2009), Regional N<sub>2</sub>O fluxes in Amazonia derived from aircraft vertical profiles, *Atmospheric Chemistry and Physics*, 9(22), 8785-8797.
- Herndon, S. C., M. S. Zahniser, D. D. Nelson, J. Shorter, J. B. McManus, R. Jimenez, C. Warneke, and J. A. de Gouw (2007), Airborne measurements of HCHO and HCOOH during the New England Air Quality Study 2004 using a pulsed quantum cascade laser spectrometer, *Journal of Geophysical Research-Atmospheres*, 112(D10), 15.
- Hirsch, A. I., A. M. Michalak, L. M. Bruhwiler, W. Peters, E. J. Dlugokencky, and P. P. Tans (2006), Inverse modeling estimates of the global nitrous oxide surface flux from 1998-2001, *Global Biogeochemical Cycles*, 20(1).
- Huang, J., et al. (2008), Estimation of regional emissions of nitrous oxide from 1997 to 2005 using multinet network measurements, a chemical transport model, and an inverse method, *Journal of Geophysical Research-Atmospheres*, 113(D17).
- Ishijima, K., et al. (2010), Stratospheric influence on the seasonal cycle of nitrous oxide in the troposphere as deduced from aircraft observations and model simulations, *Journal of Geophysical Research-Atmospheres*, 115, D20308, doi:10.1029/2009JD013322.
- Jimenez R., S. Herndon, J. H. Shorter, D. D. Nelson, J. B. McManus, and M. S. Zahniser (2005), Atmospheric trace gas measurements using a dual quantum-cascade laser mid-infrared absorption spectrometer, *Proceedings of SPIE* 5738: 318-331.
- Jimenez R., S. Park, B. C. Daube, J. B. McManus, D. D. Nelson, M. S. Zahniser, and S. C. Wofsy (2006), A new quantum-cascade laser based spectrometer for high-precision airborne CO<sub>2</sub> measurements, *WMO/GAW Reports* 168: 100-105.
- Jiang, X., W. L. Ku, R. L. Shia, Q. B. Li, J. W. Elkins, R. G. Prinn, and Y. L. Yung (2007), Seasonal cycle of N<sub>2</sub>O: Analysis of data, *Global Biogeochemical Cycles*, 21(1).

- Jin, X., and N. Gruber (2003), Offsetting the radiative benefit of ocean iron fertilization by enhancing N<sub>2</sub>O emissions, *Geophysical Research Letters*, 30(24).
- Keller, M., R. Varner, J. D. Dias, H. Silva, P. Crill, and R. C. de Oliveira (2005), Soil-atmosphere exchange of nitrous oxide, nitric oxide, methane, and carbon dioxide in logged and undisturbed forest in the Tapajos National Forest, Brazil, *Earth Interactions*, 9.
- Kort, E. A., J. Eluszkiewicz, B. B. Stephens, J. B. Miller, C. Gerbig, T. Nehrkorn, B. C. Daube, J. O. Kaplan, S. Houweling, and S. C. Wofsy (2008), Emissions of CH<sub>4</sub> and N<sub>2</sub>O over the United States and Canada based on a receptor-oriented modeling framework and COBRA-NA atmospheric observations, *Geophysical Research Letters*, 35(18).
- Kort, E. A., A. E. Andrews, E. Dlugokencky, C. Sweeney, A. Hirsch, J. Eluszkiewicz, T. Nehrkorn, A. Michalak, B. Stephens, C. Gerbig, J. B. Miller, J. Kaplan, S. Houweling, B. C. Daube, B. C. Daube, P. Tans, and S. C. Wofsy (2010), Atmospheric constraints on 2004 emissions of methane and nitrous oxide in North America from atmospheric measurements and a receptor-oriented modeling framework, *Journal of Integrative Environmental Sciences*, 7:2, 125-133, doi:10.1080/19438151003767483.
- Levin, I., T. Naegler, R. Heinz, D. Osusko, E. Cuevas, A. Engel, J. Ilmberger, R. L. Langengelds, B. Neininger, C. v. Rohden, L. P. Steele, R. Weller, D. E. Worthy, and S. A. Zimov (2010), The global SF<sub>6</sub> source inferred from long-term high precision atmospheric measurements and its comparison with emission inventories, *Atmos. Chem. Phys.*, 10, 2655-2662.
- Nevison, C. D., T. J. Lueker, and R. F. Weiss (2004), Quantifying the nitrous oxide source from coastal upwelling, *Global Biogeochemical Cycles*, 18(1).
- Nisbet, E., and R. Weiss (2010), Top-Down Versus Bottom-Up, *Science*, 328(5983), 1241-1243.
- Onogi, K., J. Tsutsui, H. Koide, M. Sakamoto, S. Kobayashi, H. Hatsushika, T. Matsumoto, N. Yamazaki, H. Kamahori, K. Takahashi, S. Kadokura, K. Wada, K. Kato, R. Oyama, T. Ose, N. Mannoji, and R. Taira (2007), The JRA-25 Reanalysis, *J. Meteor. Soc. Japan*, 85, 369-432.
- Patra, P. K., Y. Niwa, T. J. Schuck, C. A. M. Brenninkmeijer, T. Machida, H. Matsueda, Y. Sawa (2011), Carbon balance of South Asia constrained by passenger aircraft CO<sub>2</sub> measurements, *Atmos. Chem. Phys. Discuss.*, 11, 5379-5405.
- Prinn, R., D. Cunnold, R. Rasmussen, P. Simmonds, F. Alyea, A. Crawford, P. Fraser, and R. Rosen (1990), *ATMOSPHERIC EMISSIONS AND TRENDS OF*

NITROUS-OXIDE DEDUCED FROM 10 YEARS OF ALE-GAUGE DATA,  
Journal of Geophysical Research-Atmospheres, 95(D11), 18369-18385.

- Ravishankara, A. R., J. S. Daniel, and R. W. Portmann (2009), Nitrous Oxide (N<sub>2</sub>O): The Dominant Ozone-Depleting Substance Emitted in the 21st Century, *Science*, 326(5949), 123-125.
- Stephens, B. B., et al. (2007), Weak northern and strong tropical land carbon uptake from vertical profiles of atmospheric CO<sub>2</sub>, *Science*, 316(5832), 1732-1735.
- Thompson, R. L., C. Gerbig, and C. Rodenbeck (2010), A Bayesian inversion estimate of N<sub>2</sub>O emissions for western and central Europe and the assessment of aggregation errors, *Atmos. Chem. Phys. Discuss.*, 10, 26073-26115.
- Wagner-Riddle, C., A. Furon, N. L. McLaughlin, I. Lee, J. Barbeau, S. Jayasundara, G. Parkin, P. Von Bertoldi, and J. Warland (2007), Intensive measurement of nitrous oxide emissions from a corn-soybean-wheat rotation under two contrasting management systems over 5 years, *Global Change Biology*, 13(8), 1722-1736.
- Wofsy, S. C., et al. (2011), HIAPER Pole-to-Pole Observations (HIPPO): Fine grained, global scale measurements for determining rates for transport, surface emissions, and removal of climatically important atmospheric gases and aerosols, *Phil. Trans. of the Royal Society A*, in press.
- Wunch, D., P. O. Wennberg, G. C. Toon, G. Keppel-Aleks, and Y. G. Yavin (2009), Emissions of greenhouse gases from a North American megacity, *Geophysical Research Letters*, 36, 5.